Journal of Materials Research and Technology 30 (2024) 8316–8344

Contents lists available at ScienceDirect

Journal of Materials Research and Technology

journal homepage: www.elsevier.com/locate/jmrt

Current status and recent advances in magnesium-matrix syntactic foams: Preparation, mechanical properties, and corrosion behavior

A. Motaharinia [a], J.W. Drelich [b,**], J. Goldman [c], H.R. Bakhsheshi-Rad [a,*], S. Sharif [d], A.F. Ismail [e], M. Razzaghi [a]

[a] Advanced Materials Research Center, Department of Materials Engineering, Najafabad Branch, Islamic Azad University, Najafabad, Iran
[b] Department of Materials Science and Engineering, Michigan Technological University, Houghton, MI, 49931, USA
[c] Department of Biomedical Engineering, Michigan Technological University, Houghton, MI, 49931, USA
[d] Advanced Manufacturing Research Group, Faculty of Mechanical Engineering, Universiti Teknologi Malaysia, Johor Bahru, 81310, Johor, Malaysia
[e] Advanced Membrane Technology Research Center (AMTEC), Universiti Teknologi Malaysia, Johor Bahru, 81310, Johor, Malaysia

ARTICLE INFO

Keywords:
Mg-based materials
Syntactic foams
Fabrication techniques
Mechanical properties
Corrosion properties

ABSTRACT

Over the last ten years, magnesium (Mg)-based syntactic foams (SFs) have gained significant attention and their popularity continues to grow. This is because they possess unique properties such as high mechanical strength and are lightweight, making them potential candidates for applications in various industries, including aerospace, automotive, and biomedical (especially in orthopedics). This article reviews and discusses different fabrication techniques used in producing magnesium-matrix syntactic foams (Mg-MSFs). These techniques include stir casting, disintegrated melt deposition, powder metallurgy, and melt infiltration. The review comprehensively analyzes microstructure specifications, mechanical properties, and corrosion behavior exhibited by Mg-MSFs fabricated to date. The findings suggest that the properties of these foams, including microstructural characteristics, mechanical properties, and corrosion behavior, are significantly influenced by factors such as filler particle amounts and properties, Mg alloy-matrix specifications, fabrication techniques, process parameters, and post-processing treatments (such as annealing and sintering). These factors play a crucial role in determining the final characteristics of the syntactic foams. While Mg-MSFs hold substantial importance and potential, a limited body of research exists in this area. Therefore, more research is necessary to comprehensively understand these structures, which will facilitate their effective utilization in both industrial and biomedical applications.

1. Introduction

Polymeric foams (PFs) have previously achieved low densities, reaching as low as 0.026 g/cm^3, but they often suffer from low mechanical strength. The emergence of metallic foams (MFs) has introduced a new frontier in materials research. In contrast to PFs, MFs demonstrate enhanced structural integrity and increased thermal and electrical conductivity, though this comes at the cost of higher foam densities. Nevertheless, there has been successful large-scale production of lightweight MFs with densities as low as 0.05 g/cm^3 [1]. MFs are cellular structures of solid metal containing a significant volume of pores filled with gas or hollow reinforcements. The porosity of these foams generally falls within the 60%–90% range. It may take the form of isolated, interconnected, or hybrid structures that combine both isolated and interconnected porosities. MFs find extensive applications due to their outstanding properties, including remarkable specific strength, high specific stiffness, exceptional energy absorption (EA) capacity, effective vibration damping, and excellent sound attenuation, particularly in foams with isolated or hybrid porosity. Simultaneously, foams with interconnected porosity exhibit superior heat transfer capabilities, reasonable electromagnetic shielding, infiltration, and catalytic potential [2,3]. MFs have wide-ranging applications in structural, biomedical, chemical, and functional fields thanks to their exceptional properties compared to base metals. Their cell structure significantly influences the utilization of MFs, distinguishing between open-cell (interconnected pores) and closed-cell (isolated pores) foams. Primarily, aluminum (Al),

* Corresponding author. Advanced Materials Research Center, Department of Materials Engineering, Najafabad Branch, Islamic Azad University, Najafabad, Iran.
** Corresponding author.
E-mail addresses: jwdrelic@mtu.edu (J.W. Drelich), rezabakhsheshi@gmail.com, rezabakhsheshi@pmt.iaun.ac.ir (H.R. Bakhsheshi-Rad).

https://doi.org/10.1016/j.jmrt.2024.05.191
Received 15 March 2024; Received in revised form 12 May 2024; Accepted 21 May 2024
Available online 22 May 2024

steel, and iron foams have applications in the structural and aerospace industries [4,5].

In the realm of biomedical applications, metals, with their superior toughness and damage tolerance, often outshine bioactive ceramics and glasses for load-bearing orthopedic uses [5–8]. While they may not match the osteointegration and bioactivity of bioactive ceramics and glasses, metals like stainless steel, titanium (Ti), magnesium (Mg), zinc (Zn), and alloys such as Ti6Al4V are widely employed as orthopedic implants or in tissue engineering scaffolds [9–11]. A pressing need in orthopedics is the availability of biodegradable implants for clinical use. Biodegradable implants, designed to corrode and dissolve after surgery, obviate the need for a second surgery to remove the implant, thereby reducing costs and health risks for patients [12,13]. A problem arises if degradation rates in body fluids surpass the requirements for effective bone repair, resulting in premature loss of structural and mechanical integrity before complete bone healing [14]. Therefore, the enhancement of the corrosion resistance and mechanical stability particularly of Mg alloys remains a significant and ongoing challenge [15,16]. Unfortunately, Mg alloys are highly prone to corrosion, particularly in solutions containing chlorine or carbonate, owing to their low potential (−2.37 V) [17–20]. Consequently, their degradation rates in body fluids often exceed the requirements for effective bone repair, leading to premature loss of structural and mechanical integrity before complete bone healing [21]. As a result, enhancing the corrosion resistance and mechanical stability of Mg alloys has long been a significant challenge [14,22]. On the other hand, research suggests that Mg ions, a byproduct of the biodegradation of porous Mg, exhibit osteoconductive properties. These ions stimulate a significant increase in osteoblast activity surrounding the implants, potentially leading to the complete replacement of the implant with bone tissue [23–25]. Mg and its alloys also find extensive use in various industrial sectors such as automotive, aerospace, and defense due to their low density (approximately 1.74 g/cc) as it is 4.5 and 1.6 times less dense than steel and aluminum (Al), contributing to increased fuel efficiency and a reduction in greenhouse gas emissions. In the chemical industry, foams made from nickel and copper are extensively utilized [26].

Al-based alloys are widely recognized as the most commonly employed materials for producing MFs [27,28]. However, a range of other metals, including Ti [29,30], copper [31–34], steel, iron [35], nickel [36,37], Mg, and Zn, along with their alloys, have been utilized in the fabrication of MFs. Conventional foams face a challenge where increasing porosity often results in diminished strength and mechanical properties. Consequently, creating conventional foams for applications where both low density and high strength are crucial becomes nearly impossible. In response to this challenge, SFs have been developed to achieve low density concurrently with exceptional properties, including outstanding EA capabilities, high damping, and high specific strength [38–40].

SFs represent a modern iteration of traditional closed-cell foams and are a relatively recent category of composite materials. This innovative family of materials features a continuous matrix that incorporates a dispersion of hollow filler particles arranged in closely or randomly packed structures. These hollow structures can be made from various materials, including glass, ceramics, polymers, or metals. Initially utilized in marine structures for their inherent buoyancy and low moisture absorption, SFs have gained prominence. The ability to customize the mechanical and thermal properties of SFs by manipulating factors such as material selection, hollow particle volume fraction, and hollow particle wall thickness has significantly contributed to the rapid expansion of their applications [41]. Metal syntactic foams (MSF) are produced by the dispersion of hollow or porous particles within a metallic matrix. Typically, they are regarded as closed-cell cellular materials [42,43]. Metal matrix syntactic foams (MMSFs) refer to SFs created using metallic matrices. While the minimum achievable density levels are typically higher than those of standard open or closed-cell MFs, MMSFs exhibit superior mechanical properties compared to traditional MFs [44]. MMSFs have been produced with different proportions of hollow particles. Incorporating significant amounts of hollow particles, like hollow activated carbon (AC) particles or hollow fly-ash cenospheres (FACs), into metallic matrices—such as pure Mg or Mg-based alloys like AZ91 leads to the creation of MMSFs with densities ranging from 1 to 1.5 g/cm^3, positioning them in direct rivalry with Polymer Foams (PFs) for applications that require low density [45,46]. The inherently superior modulus, ductility, and melting point of MMSFs compared to PFs make them highly appealing materials [47–50].

Among various MMSFs, most studies have focused on those with Al and Al-based alloys as matrices. However, Mg presents distinct and advantageous characteristics compared to Al, including lower density, higher specific strength, biodegradability, and mechanical properties resembling natural human bone. These qualities make Mg a more suitable candidate for specific industrial applications, such as fuel efficiency, high-energy absorption, and biomedical applications. Despite these advantages, only a few studies have explored the production methods and assessed the characteristics of Mg-based matrix syntactic foams (Mg-MSFs) compared to their Al-based counterparts. This paper aims to offer a comprehensive review of fabrication techniques for Mg-MSFs, encompassing methods like stir casting, powder metallurgy (P/M), and melt infiltration, along with an analysis of the influential parameters in their fabrication. Additionally, the review extensively covers the microstructural specifications, mechanical properties, and corrosion behavior (focusing on biomedical applications) of Mg-MSFs that have been fabricated to date.

2. Filler properties

Based on the properties of the fillers, SFs can be divided into three categories: monomodal SFs, utilizing a single filler with uniform size, chemical composition, and shell porosity; bimodal SFs, incorporating two different fillers; and multimodal SFs, incorporating more than two types of reinforcements. The majority of studies conducted thus far have concentrated on creating and describing monomodal SFs. The agents that create pores in SFs can be categorized based on their overall outer shape into hollow spherical particles, often called microballoons, and pseudospherical particles known as cenospheres. It's worth noting that using microballoons tends to be more expensive than cenospheres. These particles may exhibit multi-pore or mono-pore internal morphology and can range in size from a few microns to a few millimeters. Metallic and non-metallic hollow particles can synthesize SFs [51–54]. Common non-metallic hollow particles used for fabricating SFs include glass microballoons (GMBs) (Fig. 1A(a) [55]) or hollow glass microballoons (HGMBs), fly-ash particles (Fig. 1A(b-e) [56]), hollow carbon spheres (HCSs), ceramic microballoons (CMBs) such as alumina (Fig. 1A(f) [57]), silica (SiO_2), and silicon carbide (SiC), expanded glass (EG) [42,58,59], and expanded perlite (EP) [60,61]. Some particles may feature porosity embedded in their shells, diminishing the strength of the shell and potentially causing breakage during processing. This, in turn, leads to the filling of porosities with molten Mg, resulting in a reduction of porosity volume in the SFs [51]. The substantial surface area of these particles improves the interfacial bond with the matrix material, leading to the formation of strong bonds [43]. These hollow particles are available in various sizes, ranging from nanometers (nm) to millimeters (mm), and are composed of different materials.

Due to their cost-effectiveness and widespread availability, fly ash particles are widely utilized as hollow particles in producing SFs. These fillers can be classified based on their porosity morphology into three classes: precipitators (solid or nearly solid particles), plerospheres (large particles with a compact shell containing small hollow spheres in the inner space), and cenospheres (low density hollow particles with 7–8% porosity in the shell, such as fly-ash cenospheres (FACs)) [62]. Fly ash particles are typically gray to buff in color and have diameters ranging from 0.5 to 100 μm and a density ranging from 0.4 to 1.0 g/cc [53]. Comprising predominantly aluminosilicate composition, FACs also

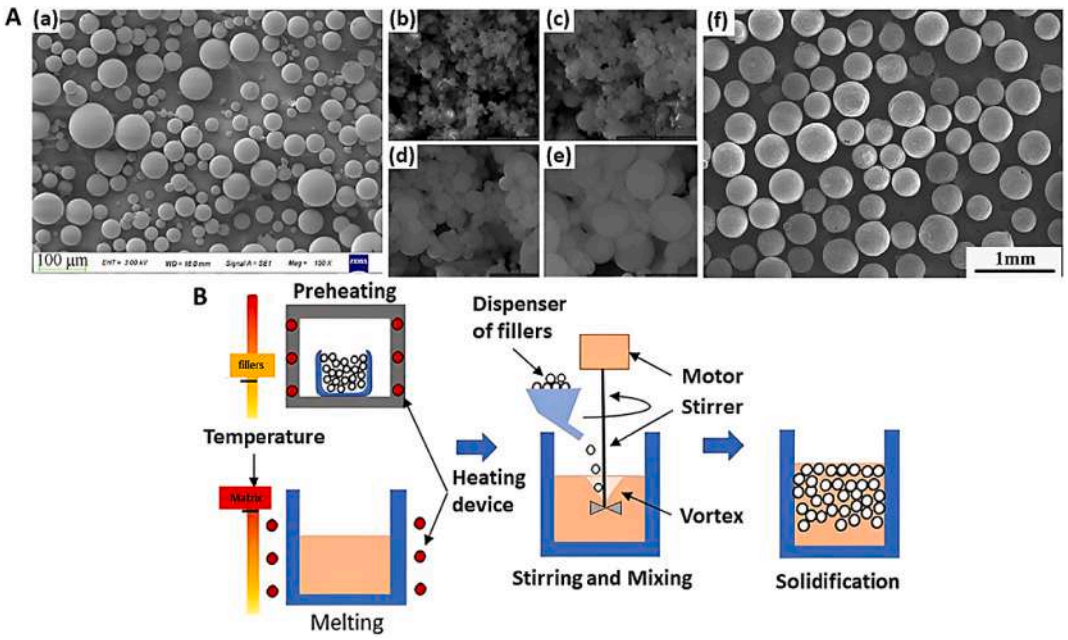

Fig. 1. (A) (a) SEM image of glass microballoons [55], Scanning electron microscope of FACs in different scales: (b) 20 000 × , (c) 50 000 × , (d) 10 0000 × , (e) 2 00 000 × [56], and (f) SEM image of the alumina (Al_2O_3) hollow spheres [57], (B) Schematic illustration of conventional stir casting method for MMSF fabrication [66].

contain numerous trace elements, posing challenges in studying the interfacial reactions and microstructures of the resulting composites [51,53]. Moreover, given that fly-ash is a by-product derived from coal-fired power plants, integrating FACs as the agent forming pores in SFs provides an efficient approach to repurposing industrial waste, concurrently leading to cost reduction in manufacturing foams. Consequently, Mg-MSFs containing FACs present themselves as attractive novel materials, thanks to their captivating physical and mechanical interactions, and their accessibility at comparably lower costs. It's important to note that FACs must undergo a conditioning process to eliminate impurities and selectively collect intact low-density particles [51]. It is worth noting that FACs have high porosity within their shell and uneven surfaces. This promotes the production of microvoids at the interface between FACs and metal matrices, such as Mg and Mg-based alloys. Furthermore, FACs have an uneven distribution in wall thickness, ranging from around 1.5 to 7 μm [63–65].

The properties and effects of the common reinforcements used to fabricate Mg-MSFs on the properties of fabricated foams and the SEM of these reinforcements are described in the following sections. For MMSFs, since generally, reinforcements have comparably lower densities than the metallic matrix, utilizing a high quantity of hollow reinforcements reduces the density of the MMSF. This makes it more suitable for applications where low density is an important factor. However, using a very high volume of hollow reinforcements can significantly reduce the mechanical properties of the MMSF or even decrease the integrity of the foam structure. The right portion of fillers should be chosen based on the mechanical and density requirements for the intended use. Furthermore, the effectiveness of the MMSF in achieving high mechanical strength and low density is highly dependent on the homogeneous distribution of the reinforcements in the metallic matrix [53–56,65].

3. Fabrication techniques

Various factors such as the chemical composition of the metallic matrix, specifications of fillers such as their shape, chemical composition, and diameter, the fabrication technique and its parameters, the aspect ratio of matrix to fillers, volume fraction of fillers in metallic matrix, and post-fabrication processing techniques such as annealing and heat treatment can significantly affect the target MMSF's properties. Among these factors, thoroughly considering fabrication techniques and accurately fine-tuning fabrication parameters is crucial since these factors can significantly impact the properties of the manufactured MMSFs [67,68]. Three primary methods are utilized in the production of MMSFs: stir casting techniques (SCTs), melt infiltration technique (MIT), and powder metallurgy (P/M) technique. The melting temperature of the metal matrix primarily dictates the choice of the optimal method. Alloys with elevated melting points, such as those based on Ti or iron (Fe), are typically processed using P/M techniques. In contrast, alloys with low to medium melting points, such as those based on Tin (Sn), Zn, Mg, or Al, are generally processed using SCTs or MITs [69,70].

3.1. Stir casting techniques (SCTs)

The conventional stir casting (CSC) method is viable for fabricating Mg-based foam/scaffolds. This technique is widely recognized as the most common, cost-effective, and straightforward among SCTs. Its simplicity stems from conceptually straightforward procedures at the process level, necessitating basic equipment such as a furnace, stirrer, recipient, and solidification mold. The CSC process involves three main steps, as shown in Fig. 1B [66]. First, there is a focus on the thermal compatibility of components, which includes melting the matrix in the furnace and preheating fillers. This preheating step enhances wettability, ensuring a more homogeneous dispersion in the metal matrix while preventing agglomeration. The second step consists of stirring the melt until an adequate vortex is achieved, with the addition of fillers at a specific rate. This stirring process is conducted for a few minutes [69–71]. The final step entails pouring the resulting mixture into a preheated mold at a specific temperature, mitigating thermal shock. It has been observed that adding particles before stirring the melt does not impact the properties of the final materials. Following the stir casting method, either slow solidification or centrifugal casting processes can be employed, resulting in a high concentration of particles in the upper section of the casting. This upper part can be utilized as the highly filled SF, while the lower part can be recycled in subsequent heats [66]. Various CSC process parameters that can significantly influence the characteristics of the produced MMSFs and their effects are outlined in Table 1.

Table 1
A summary of the effect of process parameters on the properties of MMSFs fabricated by the CSC technique.

Process parameter	Effect	Remarks	Ref.
Molten metal temperature	High effect on viscosity and particle dispersion	1. The optimal temperature should be chosen based on the best condition for particle dispersion. 2. Using very high temperatures could lead to severe erosion of the stirrer, extreme chemical interaction between the melt and particles which might lead to the penetration of molten metal into the particles, residual gas incorporation, severe oxidation of molten metal, or even its burn, can occur in the case of alloys rich in Mg, and increasing the possibility of low-density fillers floatation. 3. Employing extremely low temperatures results in elevated viscosity, making it challenging to pour the melt and causing weak and uneven dispersion of particles.	[72]
Stirrer properties	Significantly impacts the dispersion of the fillers in the melt	1. The optimum stirrer diameter is achieved when solid particles fluidize uniformly in both the central and marginal sections at an equal rate. Studies suggest that the stirrer diameter should be 0.4 times the vessel diameter (D), with the blade width falling within the range of 0.1–0.2 times D. 2. The stirrer design should enable close positioning to the crucible wall, ensuring a strong shear force and the creation of a vortex for efficient filler dispersion in the melt. 3. Excessive stirrer speeds can result in damage to the fillers' walls and the penetration of molten metal into them, while very low speeds do not yield optimal dispersion of the fillers.	[72–74]
The rate of adding fillers to the melt	Significantly influence the dispersion of fillers and the formation of clusters.	1. Adding fillers with high speed leads to heterogeneous dispersion of the filler and increases the possibility of cluster formation and agglomeration. 2. Slow rates of incorporation prolong the total duration of introducing the fillers.	[75]
Atmosphere conditions	Effect on metal matrix oxidation	1. In its molten state, metal experiences increased interaction with the atmosphere, leading to a higher oxidation rate. Mg and its alloys exhibit a higher oxidation rate than other metals like aluminum (Al) or iron (Fe), which may lead to alloy burning. 2. Using an inert gas such as argon or a combination of SF_6 and CO_2 can significantly reduce oxidation.	[73]
Material and temperature of the mold	Significantly influence both the cooling rate and the uniform distribution of fillers.	1. Preheating the mold can inhibit the floatation of the fillers in the pouring stage. 2. Cooling rate is highly affected by the mold material. Metal mold presents fast cooling rates. As an example, iron molds possess a high heat extraction capacity.	[75]

As indicated in Table 1, process parameters, which are not consistently accessible to regulate during fabrication, significantly influence the properties of the manufactured MMSF. Consequently, supplementary measures have been incorporated into the CSCs process to enhance the controllability of processing parameters and mitigate adverse occurrences, such as particle floatation or agglomeration, and/or to facilitate the attainment of desired parameters, such as achieving the target viscosity of the molten metal or uniform dispersion of filler particles. These modifications include utilizing a gentle compression on the slurry after dispersing hollow fillers in the molten metal matrix until it solidifies, incorporating a thickening agent (typically Ca) into the molten material before introducing the space holders, or employing a vacuum die casting system positioned beneath the crucible of the stirrer as the pouring mechanism. The details of these additional steps and their impact are comprehensively discussed elsewhere [66].

- **Disintegrated melt deposition (DMD) method**

DMD stands out as a distinctive and cost-effective technique combining spray processing and CSC benefits. This approach utilizes elevated superheat temperatures and lower impinging gas jet velocities to produce bulk composites and foam-based materials, particularly those based on Mg-based alloys. Notably, DMD showcases energy efficiency, resulting in a 20%–30% reduction in material wastage compared to traditional casting processes. Furthermore, it exhibits the potential to create composites with consistently distributed fillers and attain a finer grain size [76,77]. The process of producing Mg-based composites, reinforced with filler particles like Mg-MSFs using the DMD method, involves heating a layered structure of Mg chips/turnings and reinforcement powder to a temperature exceeding 650 °C. This operation is conducted in an inert atmosphere, mainly of argon, within a graphite crucible equipped with a resistance-heating furnace. The crucible is designed explicitly for bottom pouring. Once the superheat temperature is achieved, the molten slurry undergoes stirring for 5 min at around 450–465 rpm, employing a mild steel impeller with twin blades and a

pitch of 45°. This stirring process aids in the integration and homogeneous dispersion of the reinforcement particles within the metal matrix, ensuring a consistent temperature throughout the process. The impeller is predominantly coated with Zirtex 25, which contains 86% ZrO_2, 8.8% Y_2O_3, 3.6% SiO_2, 1.2% K_2O, and Na_2O, along with 0.3% trace inorganic components. This coating aims to prevent any iron contamination in the molten metal. Subsequently, the molten metal is discharged through a 10 mm diameter orifice at the crucible's base. To disintegrate the composite melt, two argon gas jets are oriented perpendicular to the molten stream, leading to its deposition onto a metallic substrate [63,77–80]. This method facilitates the creation of either Mg-based composites or Mg-MSFs, depending on the nature of the particles utilized as reinforcements, whether they are filled or hollow. Certain challenges need to be addressed when employing the DMD technique (Fig. 2A [78]), including the potential for oxidation and contamination of the molten metal, susceptibility to thermal shock, residual stresses within the composite, and challenges related to large-scale production and intricate shapes [81,82]. These factors can remarkably impact the resulting Mg-based foam's mechanical characteristics and corrosion resistance. It's worth noting that DMD can be viewed as a modified version of CSC. Following the DMD process, hot extrusion can be employed to attain the desired shape for the foam or composite.

- **Compo-casting**

Compo-casting, a method akin to CSC, involves introducing particles into a metal during a semi-solid phase rather than in its liquid state [83]. Huang and Yu [84] employed this technique to create AZ91D Mg alloy/FAC composites. Initially, they heated the Mg alloy to 720 °C in an electric furnace crucible and gradually cooled it to 590 °C to achieve a semi-solid phase. Subsequently, FAC particles were introduced into the semi-solid Mg-based matrix, and the mixture was stirred to ensure a uniform dispersion of fillers within the molten metal. In the final step, the slurry is quickly reheated to 720 °C for 15 min, cast into a preheated mold at 200 °C, and left to cool slowly, resulting in the fabricated Mg-based composite.

3.2. Melt infiltration technique (MIT)

As previously discussed, the MIT is primarily employed for alloys with lower melting points, such as Mg. This process entails establishing a particle bed within a mold, melting the metal, and infiltrating it into the bed under either high pressure, vacuum, or a combination of both (Fig. 2B [45]). This infiltration can occur in either an upward or downward direction. Subsequently, the sample is cooled to complete the process [85]. It is important to highlight that precise control over the particle preheat temperature and melt superheat temperature is essential to avoid incomplete infiltration and minimize the risk of freeze choking of the melt. Accurately controlling these temperatures plays a pivotal role in ensuring the success of the infiltration process [86,87].

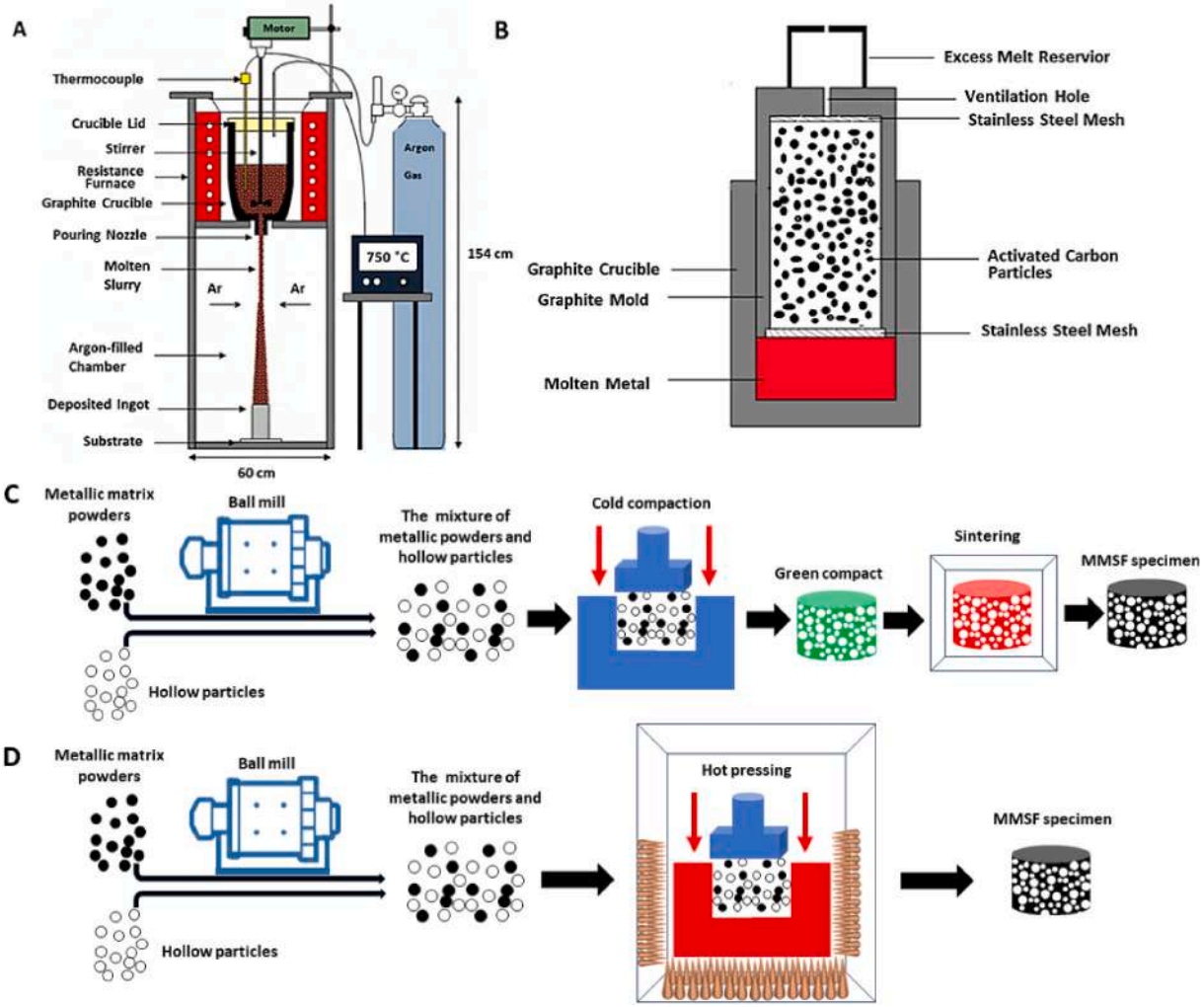

Fig. 2. (A) Schematic illustration of the setup of the DMD technique [78], (B) Illustration of the counter gravity infiltration casting process [45], (C) a schematic illustration of powder metallurgy technique utilizing cold compaction, and (D) schematic illustration of powder metallurgy technique utilizing cold compaction.

Although MIT presents numerous advantages, including the capability to produce metal matrix composites (MMCs) with high volume fractions of fillers and uniform dispersion of fillers without additional processing steps [1,88,89], it also has some limitations that should be mentioned. These include the inability to produce MMSFs with low volume fractions of particles [87,90], shape ability constraints due to the technique's limitation to infiltrate only thin beds of fillers and the inability of the infiltration mold to support complex geometries [91], the possibility of particle fracture and penetration of the molten metal into particles under MIT with high-pressure methods, and the potential need for additional costs or specialized equipment to prepare special preforms of fillers [67].

Attaining successful infiltration of metallic-based materials like Mg and its alloys without filler particle breakage necessitates maintaining a minimum threshold pressure within the infiltrating system. This pressure can be determined theoretically or experimentally customized for specific Mg-MSF. The Young-Laplace equation is a fundamental approach among the various models developed. It relies on a hydraulic radius influenced by the shape and volume fraction of the fillers. By this equation, when the necessary threshold pressure is below 1 bar, it can be produced using a vacuum instead of applying additional pressure [92–94]. Furthermore, the Young-Laplace equation incorporates considerations for the filler's surface tension and wetting angle. The wettability of fillers, in particular, plays a crucial role in determining the threshold pressure of infiltration. In cases where fillers exhibit low wetting properties, applying external pressure becomes essential to ensure the proper filling of interstitial spaces within the bed of fillers or preform. Alternatively, a strategy to address this challenge involves coating the particles with materials that enhance their wettability with the molten metallic matrix [87,95]. Pre-forms crafted from fillers exhibiting favorable wetting properties can undergo spontaneous filling with molten metallic matrix. This spontaneous filling occurs due to the metallostatic weight of the molten metallic matrix, enabling the natural flow and penetration into the pre-form [67]. Significantly, MIT finds application in infiltrating molten metal into a bed of fillers, facilitating the fabrication of MMSFs like Mg-MSFs. Various methods employed in these techniques encompass centrifugal infiltration, counter-gravity pressure infiltration (assisted by gas or mechanically), downward pressure infiltration (assisted by gas or mechanically), and downward pressure-less infiltration. Comprehensive descriptions of these techniques can be found elsewhere [67]. Within these techniques, counter-gravity pressure infiltration, also recognized as sub-atmospheric pressure infiltration, stands out as the most commonly employed method for fabricating Mg-MSFs. The potential for Mg ignition during the fabrication of Mg-MSFs using SCTs and MIT is heightened due to the elevated temperatures involved in these techniques. Several methods can be employed to address this challenge. One approach involves enhancing the ignition properties of Mg by incorporating minute quantities of rare earth elements, like Yttrium (Y). Another effective strategy is the addition of nano-reinforcements like La_2O_3 and ZnO to the Mg or Mg-based alloy matrix [96]. Parande et al. [97] demonstrated that adding 2 vol% of SiO_2 nano-particulates to monolithic pure Mg led to a notable increase in the ignition temperature, reaching 611 °C. This elevation represents an approximately 20 °C improvement compared to the ignition temperatures observed in pure Mg and AZ31 alloy.

3.3. Powder metallurgy (P/M) technique

While the P/M technique is typically favored for metals with high melting points, it is applicable in the fabrication of Mg and Mg-MSFs. Although Mg and its alloys inherently have low melting points, the P/M method demonstrates effectiveness due to addressing challenges associated with liquid Mg/Mg-based alloys, such as high vapor pressure and susceptibility to oxidation, which are common side effects in SCTs and MITs. The key lies in employing lower temperatures during fabrication [98–100]. Expanding upon the benefits of the P/M technique, it allows for incorporating diverse reinforcement particles with varying volume fractions and diameters. Nonetheless, it is essential to acknowledge certain drawbacks. Notably, there is a risk of substantial fracture of weak hollow particles (fillers) during the compaction stage, mainly when dealing with high-volume filler fractions. The P/M technique comprises three primary steps: homogeneous mixing of components, compaction of the mix to make a green compact, and subsequent sintering of the compacted part [101].

The P/M process begins by combining filler particles with metal matrix powder to create a mixture with uniform component dispersion. Component characteristics and blending equipment must match to achieve a uniform and more homogeneous distribution. Powder characteristics—particle size, shape, density, and surface features—determine mixing equipment [102]. This is done with various mixing devices, such as V-type, double cone, slant cone, and cube tumble blenders. Ribbon or screw blenders, which have minimal shear, should mix hollow particles that are sensitive to shear forces. Stirrers are mainly used to improve the dispersion and homogeneity of fillers and the mixture. Although stirrers with high speeds enhance homogeneous filler dispersion, extreme speeds may break filler particles while mixing, which should be avoided. It's also important to note that adding a binder can improve the metallic matrix powder and reinforcements' mixing uniformity. The characteristics of the target metallic powder and reinforcing particles should be considered while choosing the binder [102,103]. Among mixing equipment, using a ball mill could be regarded as the most commonly used method in Mg-based foam fabrication by the P/M technique [104–106].

In the second step, the target metal powder and filler particles are combined and compressed inside an appropriate die to create a specimen replicating the die's internal geometry. The term "green compact" refers to this compressed mixture. Both hot and cold compaction processes can be utilized at this stage. Hot compaction, also known as hot pressing, is a two-step process involving high temperatures to compress a blend of powders, followed by sintering. This method effectively combines compaction and sintering within a single chamber. Maintaining a temperature lower than the critical melting points of the metallic matrix and reinforcement powders during hot compaction is crucial to ensure proper blending without melting [101–107]. In contrast, cold compaction takes place at ambient temperature, and the resulting green compact undergoes sintering only at the subsequent sintering stage. Moreover, when selecting the appropriate technique, the characteristics of the matrix/reinforcement powder mixture must be carefully considered. It is crucial to avoid applying excessive mechanical force during the compaction phase, as it may lead to the fracture of reinforcement shells. This phenomenon needs to be prevented in both hot and cold compaction processes [101,107]. Schematic illustrations of the P/M technique utilizing cold compaction and hot pressing are provided in Fig. 2C and D, respectively.

The third stage involves sintering, a crucial heat treatment that leads to the process that transforms a mixture of powders into a functional product with the desired microstructure, especially applicable to metallic-based alloys such as Mg-based alloys. Sintering is necessary to provide sufficient integrity and particle fusion in Mg-MSFs, which increases the mechanical properties of Mg-MSFs. The sintering process can be categorized into four main types: solid-state, viscous, liquid-phase, and pressure-assisted. Solid-state sintering involves fully densifying the powder compact at the designated sintering temperature without any liquid phase present. On the other hand, liquid-phase sintering occurs when a liquid phase is present in the powder compact during the sintering process. Viscous sintering involves the presence of a viscous liquid phase throughout the process. On the other hand, pressure-assisted sintering includes applying external pressure during the sintering process. Pressure-assisted sintering encompasses a range of methods, including uniaxial hot pressing, hot isostatic pressing, sinter forging, and spark plasma sintering (SPS). Each technique plays a distinct role in achieving specific material properties and product

characteristics during the sintering stage [46,108,109].

Based on the sintering agent, the sintering process can be categorized into four types.

1) Conventional sintering: This method relies solely on heat for the sintering process, thus requiring elevated temperatures for its execution.
2) Hot pressing: This process employs heat and external pressure for the sintering process, as discussed earlier.
3) Microwave sintering (MWS): In this method, the primary mechanism for generating the required heat for sintering is the interaction between electromagnetic waves and dipoles in the material. The material involved can be the substrate itself or an additional susceptor. MWS offers several advantages over conventional sintering and hot-pressing techniques. It is notably faster, consumes less energy, and does not necessitate mechanical pressure. These advantages significantly mitigate the risks of undesirable effects, such as filler particle fracture or unintended interfacial reactions between the matrix and filler particles [110,111]. Recent research conducted by Batienkov et al. [112] extensively elucidated the MWS of metallic powders, detailing its parameters and distinctive features.
4) Hybrid microwave sintering: This method employs a combination of microwaves and other elements such as heat to sinter the green compact. The environmentally friendly nature of hybrid MWS contributes to enhanced end-application properties, along with significant reductions in processing time and costs. The integration of the P/M process with hybrid microwave sintering represents a prevalent processing approach for fabricating Mg-MSFs, as demonstrated in various studies [113].

In the context of Mg-MSFs, silicon carbide (SiC) stands out as one of the susceptors suitable for MWS or hybrid MWS. To mitigate the oxidation of Mg during the sintering stage, an inert gas, typically argon, is commonly utilized in the surrounding environment [114]. Subsequently, the produced foam can be extruded to attain the desired shape [77,113]. It's crucial to emphasize that extended sintering cycles lasting several hours, as seen in traditional sintering techniques, not only escalate manufacturing expenses but can also result in the formation of undesirable brittle products at the interface between the matrix and filler particles.

AZ (aluminum-zinc) and ZC (zinc-copper) Mg-based alloys stand out as the most prevalent Mg-based alloys employed for the fabrication of Mg-MSFs through various described methods [46,47]. Notably, the techniques elucidated in this paper are adaptable for creating foams with open-pore structures. In fabricating such foams, particles serving as reinforcements in the SFs must be designated as pore-making agents and subsequently eliminated post-fabrication. These particles can be removed through diverse methods, including heating [115–117] or employing a suitable electrolyte solution [118]. The selection of the technique for particle (pore-making agents) removal should align with the properties and characteristics of the particles involved. Table 2 summarizes the SFs with different Mg-based matrixes, along with the information on the fabrication method and fillers.

According to the described techniques, the main drawback of SCTs and MITs is that they apply higher temperatures than the P/M technique. This can increase the possibility of Mg-based matrix ignition and a severe reaction between the molten matrix and fillers, leading to hollow filler particle penetration. On the other hand, although in the P/M technique lower temperatures are applied, the applied physical pressure in this technique can lead to hollow filler particle fracture. The pros and cons of each fabrication technique are listed in Table 3 [135].

Table 2
Various SFs with different Mg-based matrixes and filler properties, fabricated by SCT, MIT, and P/M processes.

Fabrication technique	Matrix material	Filler properties	Ref.
Stir casting	ZC63 Mg-alloy	Fly ash microballoons Mean particle diameter = 100 μm Density = 0.6 g/cm^3	[72]
Stir casting	AZ91D Mg-alloy	Hollow glass microspheres Filler percentage = 15, 20, and 23 wt% Mean particle diameter = 45 μm Density = 0.37 g/cc	[73]
Stir casting	AZ31 Mg-alloy	Hollow alumina microspheres Filler percentage = 5, 10, and 15 vol% Mean bubble diameter = 0.3–0.6 mm	[119]
DMD	Pure Mg	Hollow glass micro balloons Filler percentage = 5, 15, and 25 wt% Mean particle diameter = 11 μm Density = 1.05 g/cc	[79, 80]
DMD	Pure Mg	HSNS Filler percentage = 0.5, 1.0, 1.5 and 2.0 vol% Mean particle diameter = ~10–20 nm	[120]
DMD	Pure Mg	HSNS Filler percentage = 0.5, 1.0, 1.5 and 2.0 vol%	[121]
DMD	Pure Mg	FACs Filler percentage = 0.5, 1.0, 1.5 and 2.0 vol% Mean particle diameter = 60 μm Density = ~0.45 g/cc	[63]
DMD	Pure Mg	HSNS Filler percentage = 0.5, 1.0, and 1.5 vol% Mean particle diameter = 10–20 nm	[122]
Compo-casting	AZ91D Mg-alloy	FACs Filler percentage = 5 wt % Average particles diameter = ~100 μm	[84]
Pressure infiltration	AZ91 Mg-alloy	spherical FACs Average particle diameter = ~180–250 μm	[123]
Pressure infiltration	Cp-Mg, AM20, AM50, and AZ91 Mg-alloys	Hollow sintered alumina spheres Filler percentage = 63 vol% Using fillers with different diameters = 2.8 mm with wall thickness of 133 or 181 μm and 3.7 mm with 115 or 150 μm	[85]
Pressure infiltration	$Mg_{60}Cu_{21}Ag_7Gd_{12}$	Iron hollow spheres Average filler percentage = 62 vol% Mean particle diameter = 1.87 ± 0.10 mm with a wall thickness of 41.5 μm Net sphere density = 1.0 ± 0.1 g/cm^3	[124]

(continued on next page)

Table 2 (*continued*)

Fabrication technique	Matrix material	Filler properties	Ref.
Sub-atmospheric Pressure infiltration	AZ91 Mg-alloy	SiC hollow particles Filler percentage = 50 vol% particle nominal diameter = 1 mm with a particle wall thickness of 70 μm particle bulk Density = 0.7 g/cm^3	[125]
Sub-atmospheric Pressure infiltration	AZ91D Mg-alloy	Hollow alumina spheres Filler percentage = 50 vol% Reinforcement particles diameter and their bulk densities = particles with three different diameters (0.106–0.212 mm with the bulk density of 2.03 g/cc, 0.212–0.425 mm with the bulk density of 1.33 g/cc, and 0.425–0.500 mm with the bulk density of 1.24 g/cc)	[126]
Sub-atmospheric Pressure infiltration	AZ91D Mg-alloy	SiC hollow particles Average particles diameter = 2 mm Average particle wall thickness = 130 μm	[127]
Gas pressure infiltration technique	Pure Mg	Active carbon hollow spheres Average particles diameter = 534 μm	[128]
Counter-gravity infiltration	AZ91 Mg-alloy	Active carbon particles Filler percentage = 58.75 vol% Particles bulk density = 0.47 g/cm^3	[45]
Pressure infiltration	Pure Mg	Hollow ceramic spheres (comprising 35 wt% Al_2O_3, 45 wt% SiO_2 and 20 wt% mullite) Particles outer diameter = 1.45 mm Particles wall thickness = 250 μm	[129]
Low-pressure infiltration	Commercially pure Mg	G1.45 Globocer hollow spheres (consisting of 35 wt% Al_2O_3, 45 wt% SiO_2 and 20 wt% mullite) Particles outer diameter = 1.45 mm Particles wall thickness = 250 μm	[130]
Low-pressure infiltration	Commercially pure Mg	G3.83 Globocer hollow spheres (consisting of 99.7% Al_2O_3; 0.3% other oxides) Particles outer diameter = 3.83 mm Particles wall thickness = 150 μm	[130]
P/M + hybrid MWS followed by a hot extrusion process	Mg powder with a size of 60–300 μm	FACs Filler percentage = varied from 5 to 15 wt %. Average particles diameter = ~50 μm	[113]
P/M + rapid MWS	AZ61 Mg-alloy powder with a size of 150–300 μm	A combination of both leachable spherical carbamide granules and hollow fly ash microspheres Filler percentage Carbamide granules properties Diameter: 0.50–0.90 mm fly ash microsphere properties Density: 0.70 g/cm^3 Diameter = Ø 100–250 μm Wall thickness = 16.08 ± 7.70 μm	[131]
P/M + MWS	AZ61 Mg-alloy powder with a size of ~50 μm	Hollow fly ash cenosphere particles Filler percentage = 20, 30, and 40 vol%. Average particles diameter = ~50 μm Particles bulk density = 0.70 g/cm^3	[132]
P/M + hybrid MWS	Mg powder with a purity of 98.5% and a size ranging from 60 to 300 μm	Hollow spherical GMBs (soda-lime borosilicate glass, iM30K) Filler percentage = 5, 10, and 20 wt% Average Particles size = 16 ± 6 μm Particles density = ~0.6 g/cc Particles crush strength = 193 MPa	[133]
P/M with hot extrusion followed by DMD techniques	Mg turnings with 99.9% purity	HGMBs Filler percentage = 20 wt% Particles diameter = 11 μm Particles density = ~1.05 g/cc	[76]
Vacuum die casting	AZ91D Mg-alloy	Hollow glass microspheres Filler percentage = 10 wt%, 15 wt%, and 20 wt % Particles diameter = 45 μm, 55 μm, and 65 μm.	[134]

Table 3
The key information of fabrication technique of particle reinforced metal foams [135].

Technique	Main advantages	Main drawbacks
Stir casting	1. Simplicity 2. Low cost	1 Limited volume fraction of additives 2. Inhomogeneous distribution of particles
Gas injection	1. Simple and straightforward 2 Mass production	1. Hard to control foaming process 2. Nonuniform cell sizes
Powder metallurgy	1. Homogenous microstructure	1. Unsuitable for mass production 2. The equipment is relatively expensive
Infiltration	1. Homogenous foam microstructure and distribution of particle 2. Suitable for various particle sizes and volume fraction of particles	1. Relatively complicated and expensive

4. Properties

4.1. Microstructure properties

The microstructural features directly and substantially impact the

mechanical properties and EA characteristics of MMSFs. The microstructural attributes of MMSFs can be adjusted through the fabrication technique and its parameters, the chemical composition and components of the metallic matrix, and the reinforcement parameters and features such as chemical composition, wall thickness, volume fraction, and size distribution. Through these adjustments, both the overall microstructural and mechanical characteristics can be tailored and regulated [87,114,136].

Typically, MMSFs are composed of isolated pores. The microstructure of an MMSF comprises a metallic matrix as the continuous phase, primary porosities created by the internal space of hollow particles (fillers), and matrix voids primarily formed at the interface of the outer surface of fillers and the metallic matrix. The origin of these matrix voids lies in the heterogeneous structure of the filler shells, resulting from microporosities in the filler shell. Additionally, the production of gas from fractured particles and the shrinkage effects of the metallic matrix can further contribute to the formation of matrix voids (Fig. 3A [47]). These microvoids, although generally regarded as unfavorable occurrences due to their potential to lead to unpredictable reductions in the mechanical properties of MMSFs, can be advantages in applications where achieving low density is the primary objective, the presence of these microvoids can be advantageous, provided that the necessary mechanical properties are still met [47,136].

SCTs have been employed in various studies to fabricate Mg-MSFs as it is a straightforward process. Daoud et al. [72] utilized this method to fabricate a composite of ZC63 Mg-based alloys reinforced with 10%, 20%, and 25% volume fractions of fly ash microballoons. The microstructural evaluation revealed that the microstructure of the unreinforced ZC63 in its as-cast condition exhibited a typical dendritic structure (Fig. 3B(a)), consisting of α-Mg and Mg $(Zn, Cu)_2$ eutectic phases, Cu_5Zn_8, and CuMnZn at the interdendritic regions. In the case of ZC63 composite foams, uniform dispersion of microballoons within the matrix was observed, with no signs of fly ash clusters or residual porosity (Fig. 3B(b-e)). Moreover, composites of ZC63 Mg-based alloy and fly ash showcased a cellular dendritic structure, as illustrated in Fig. 3B(f). Within this structure, some fly ash microballoons were observed to be filled by the Mg-alloy matrix. An examination of the interface of the composite revealed that heterogeneous nucleation of eutectic and other intermetallic phases occurred on the fly-ash microballoons (Fig. 3C) [72]. Moreover, the key interfacial phase identified between fly ash and ZC63-Mg alloy was determined to be MgO. This recognition of MgO played a pivotal role in promoting the wetting process and the smooth integration of the spheres into the Mg-based matrix [72].

In a similar study, an AZ91D Mg-based SF reinforced with hollow glass microspheres (HGM), characterized by particle size and density of 45 μm and 0.37 g/cc, respectively, was successfully developed using SCT [73]. Microstructural analysis revealed a homogenous dispersion of HGM within the Mg-based matrix, with no evidence of clustering. The solid solution of the Mg-based matrix exhibited acicular precipitates of $Mg_{17}Al_{12}$ particulates at the grain boundaries (GBs), as presented in Fig. 4 [73]. The SF composition included Mg_2Si, Al–Mn, and B_2O_3 phases. The existence of borosilicate spherules at the HGM/matrix interface indicated the formation of $Mg_{17}Al_{12}$, Al–Mn, Mg_2Si, B_2O_3, and CaO [73].

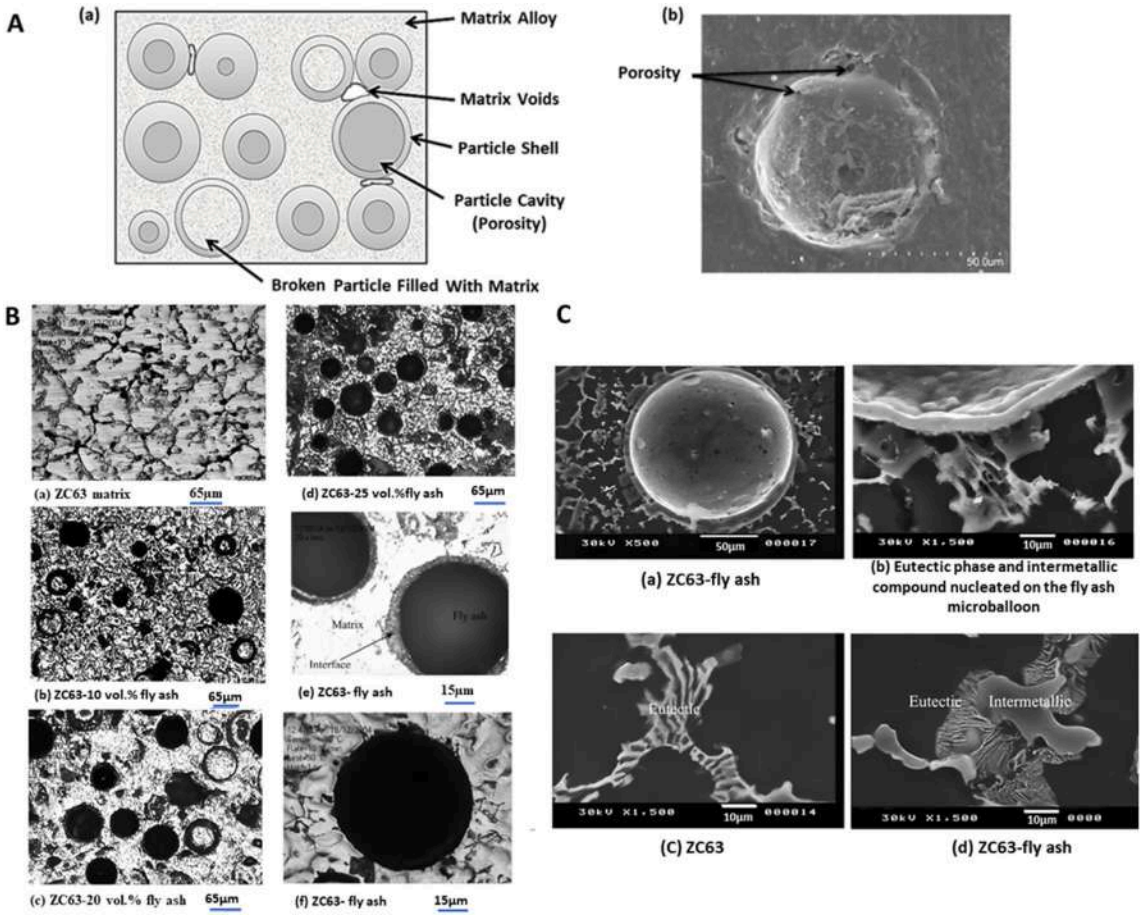

Fig. 3. (A) (a) Schematic diagram of SF microstructure with different phases and two types of cavities (main pores and matrix voids), (b) Scanning electron micrograph of AZ91D/FACs composite, where porosity and defects are visible in the FAC shell [47], (B) Microstructure optical images of ZC63 matrix and its composites, with panels (a–d) providing an overview and higher magnification views displaying the interface between the ZC63 Mg-based alloy and microballoons (e, f), (C) Scanning electron microscope (SEM) micrographs illustrating the microstructure of the ZC63 Mg alloy and its composite [72].

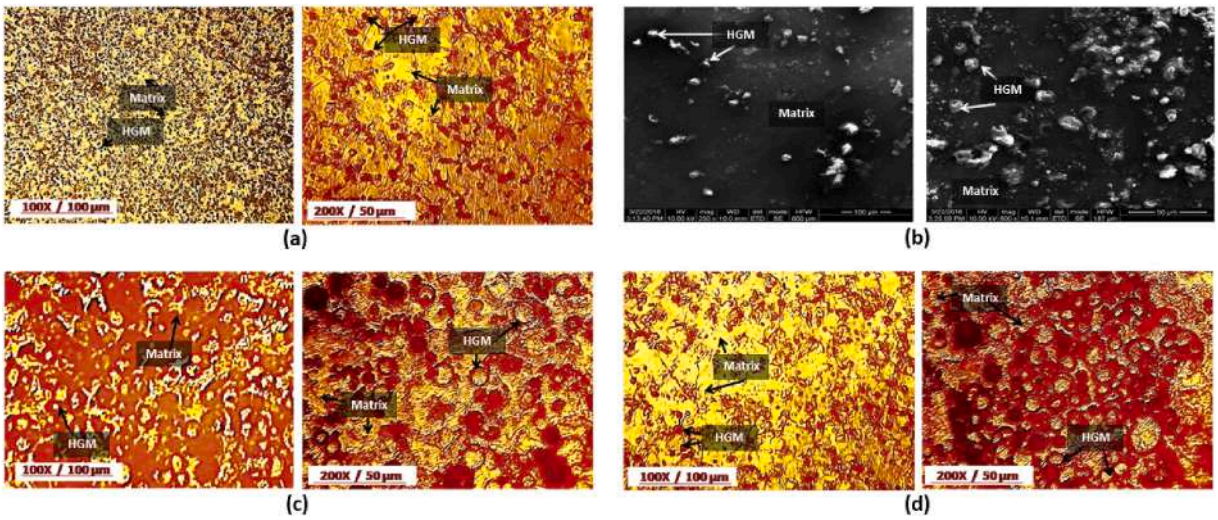

Fig. 4. (a) Microstructural depiction of AZ91D/HGM SF containing 15% HGM, (b) SEM micrographs illustrating 15% HGM with AZ91D alloy, (c) Microstructural representation of AZ91D/HGM SF incorporating 20% HGM, and (d) Microstructure image of AZ91D/HGM SF reinforced with 23% HGM [73].

The DMD techniques have found extensive application in the fabrication of Mg-based SFs. Manakari et al. [79] utilized pure Mg and GMBs with an average diameter of 11 μm and a density of approximately 1.05 g/cc to produce Mg-MSFs through this method, achieving Mg-based SFs with a density range of 1.47–1.67 g/cc. Microstructural analysis of the samples showed a homogenous dispersion of intact GMBs with an outer diameter of 8–13 μm and notable variations in morphology (Fig. 5A(a)), fractured GMBs (Fig. 5A(b)) resulting from interface reactions between the Mg-based matrix and GMBs, as well as processing parameters, and the presence of microvoids (Fig. 5A(b)), along with the presence of a secondary phase (Mg_2Si) exhibiting two different morphologies, namely dendritic crystals with a size range of 3–5 μm (Fig. 5A(c)) and polygons at the particle/Mg matrix interface [79]. In another investigation, Qureshi et al. [121] employed the same manufacturing process to create Mg-MSFs using varying percentages (0.5–2.0 vol%) of hollow silica nano-spheres (HSNS) as fillers. Nguyen et al. [63] applied a similar manufacturing technique to produce Mg-MSFs composed of Mg and different weight percentages of FACs (5-15 wt%). The microstructural evaluation indicated that many FACs were broken during casting and filled with molten Mg. Furthermore, a uniform distribution of FACs was observed in all instances, with the quantities of secondary phases (Mg_2Si and MgO) increasing proportionally with the reinforcement content. Moreover, microvoids at the FACs/Mg matrix interface were ascertained [63].

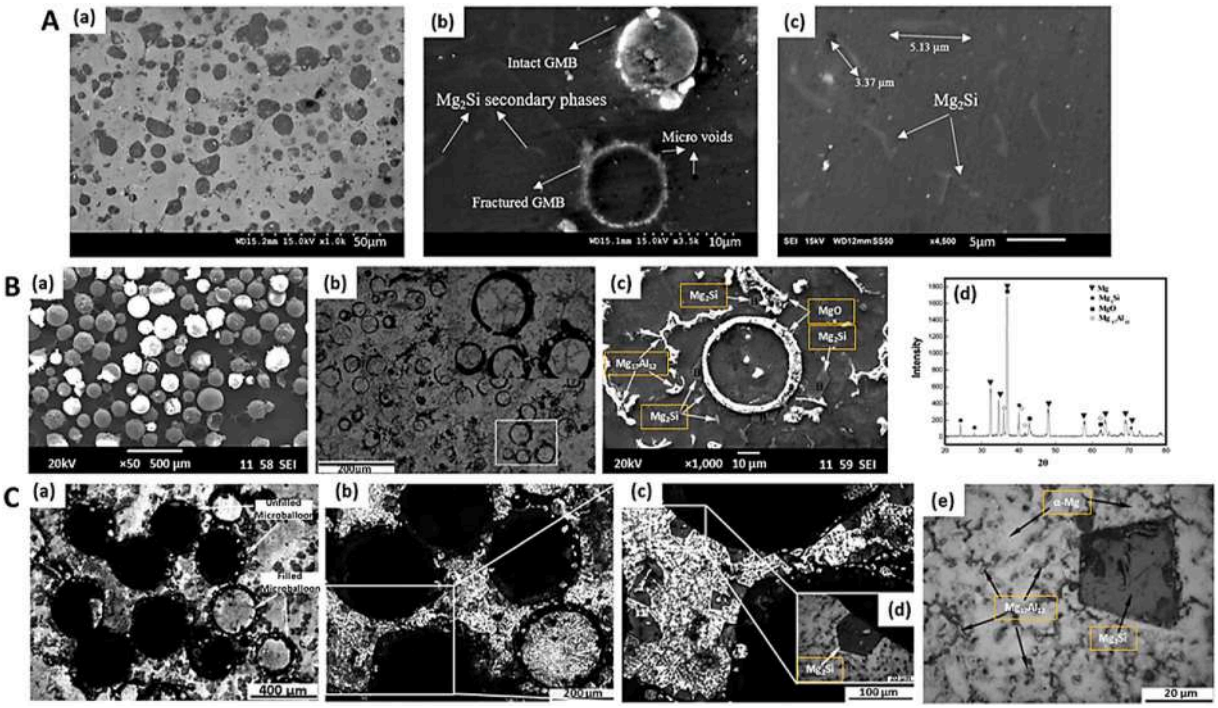

Fig. 5. (A) (a) Microstructure of Mg-15 wt% GMB foam, (b) Uniform wall thickness observed in GMB, and (c) Mg_2Si dendrites within the Mg matrix [79]; (B)(a) Morphology of FAC, (b) and (c) Microstructures of AZ91D/FAC composites, and (d) XRD pattern of AZ91D/FAC composites [84], (C)(a) Optical microscopy image of AZ91-microballoon composites, (b, c, and d) Microstructure of the composites after etching process with various magnifications, and (e) Primary Mg_2Si in Mg alloy matrix [123].

Huang and Yu [84] manufactured AZ91D/FAC composites using the compo-casting method, incorporating in-situ Mg_2Si and MgO reinforcements by adding 5 wt% FAC (Fig. 5B(a)) to AZ91D Mg-alloy. Microstructural analysis showed a uniform dispersion of filler particulates in the matrix, with most of them infiltrated by the matrix alloy (Fig. 5B(b)) [84]. Additionally, it was illustrated that the in-situ formation of Mg_2Si and MgO compounds predominantly occurred on the surfaces of FAC particles, with a minor amount of Mg_2Si developed within the matrix (Fig. 5B(c)). The main Mg_2Si structures displayed polygonal morphologies with an average size of 15 μm, showcasing distinctive growth edge characteristics. Except for the Mg_2Si and MgO phases, the existence of the $Mg_{17}Al_{12}$ and α-Mg phases was confirmed by the XRD pattern (Fig. 5B(d)) [84]. In a similar study, Liu et al. [123] fabricated in situ Mg_2Si reinforced AZ91 Mg-based SF with a density of 1.23 g/cm^3 and a porosity of 45.6–48.9% by pressure-assisted infiltration of a preform of FACs. It was indicated that although many FACs were hollow, some were penetrated by molten AZ91 Mg-based alloy (Fig. 5C(a)). Additionally, it was demonstrated that Mg_2Si is a reaction product between Mg and FAC, and it can grow from the FAC shell into the matrix (Fig. 5C(b-d)). Moreover, some Mg_2Si regions surrounded by α-Mg and a discontinuous net of the $Mg_{17}Al_{12}$ phase were seen in the matrix, as depicted in Fig. 5C(e). The dominant morphology of Mg_2Si components was polygonal, although some regions exhibited a dendritic crystal morphology [123].

In 1998, by employing MIT, Hartmaan et al. [85] pioneered the fabrication of Mg- and Mg-based alloy matrix SFs. They utilized an upward vacuum-assisted infiltration process, incorporating hollow sintered alumina spheres with varying diameters as fillers, and employed four different Mg alloys as metal matrices. They successfully fabricated reproducible Mg-based SFs featuring a homogeneous and isotropic structure. Additionally, their research identified a threshold pressure beyond which cracks emerged, followed by sphere penetration. In a separate investigation, utilizing a sub-atmospheric pressure infiltration method, Newsome and collaborators [126] fabricated AZ91D Mg-based SFs by incorporating Al_2O_3 hollow particles as fillers with three different size ranges: 0.106–0.212 mm, 0.212–0.425 mm, and 0.425–0.500 mm. Microstructural analysis of the as-cast specimens revealed a uniform dispersion of hollow particles within the metal matrix, entirely encapsulated. Furthermore, minimal to negligible porosity was observed in the matrix between adjacent hollow particles. The analysis also identified the presence of several reinforcement particles that had fractured and were subsequently infiltrated by the matrix alloy (Fig. 6A) [126]. In a comparable study, Rivero et al. [125] employed a sub-atmospheric pressure infiltration process to produce AZ91 Mg-alloy without any reinforcements and AZ91 Mg-MSFs strengthened by nearly 50 vol% of hollow silicon carbide spheres (HSCS) with a nominal diameter of 1 mm and a wall thickness of 70 μm, all under identical conditions. The microstructural evaluation of the fabricated AZ91 Mg alloy revealed a dendritic structure consisting of α-Mg dendrites surrounded by both coarse and lamellar intermetallics, predominantly $Mg_{17}Al_{12}$, along with observed interdendritic porosity. In the case of the fabricated AZ91/HSCS SFs, the microstructural evaluation indicated the homogenous dispersion of HSCS, fully encapsulated in the matrix between the hollow spheres. Additionally, some spheres exhibited cracks, likely occurring during or after solidification because of the mismatch in the coefficient of thermal expansion (CTE) of the matrix and HSCSs, the spheres had minimal infiltration. The microstructure of Mg-AZ91/HSCS SF revealed refinement compared to the monolithic matrix cast under identical conditions. This refinement was attributed to the restricted solidification of the liquid in the spaces between spheres. Additionally, intermetallic containing small amounts of Si were observed, possibly resulting from the reaction between HSCS and the alloy matrix [125]. In

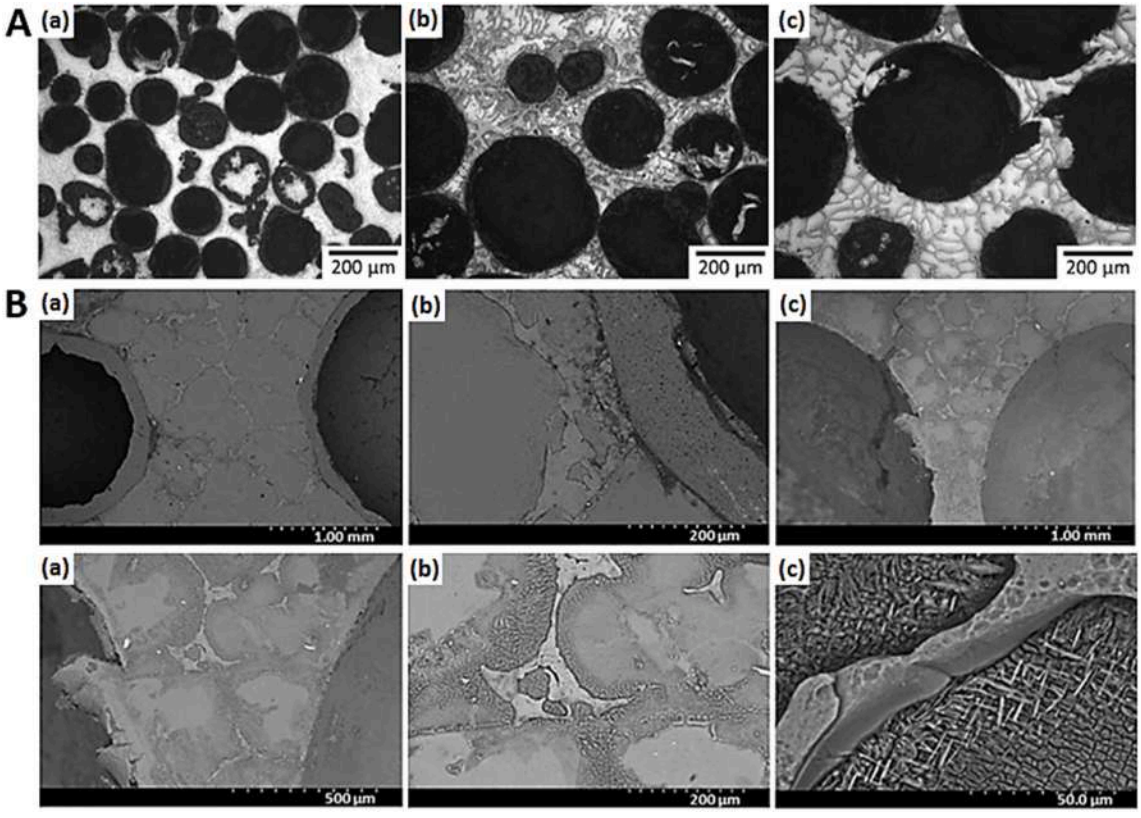

Fig. 6. (A) Microstructure images of AZ91D-Al_2O_3 Mg-MSF containing hollow particulates with different sizes with dimeters in the range of (a) 106–212 μm; (b) 212–425 μm; and (c) 425–500 μm [126]. In Fig. 6B, back-scattered SEM micrographs illustrate AZ91D/SiC hollow particles SF, featuring (a) HSCS, (b) particle-matrix interface, (c–d) the grain structure and the precipitates oriented along the GBs in the α-Mg matrix, (e) a precipitate in the matrix, and (f) the eutectic mixture surrounding it (adapted from Ref. [127]).

a parallel study, Anantharaman et al. [127] manufactured low-density AZ91D Mg-alloy-based SFs, with a density of 0.97 g/cc, by dispersing HSCS (average diameter of 2 mm and wall thickness of 130 μm) (Fig. 6B (a)) in the AZ91D Mg-alloy matrix employing a sub-atmospheric pressure infiltration technique. Microstructural evaluation of the as-cast SFs revealed a continuous interface between HSCS and the matrix alloy with no observed porosity (Fig. 6B(b)). The primary composition of AZ91D included an α-Mg phase, with intermetallic $Mg_{17}Al_{12}$ β-phase precipitates dispersed along the GBs of the α-Mg phase in the as-cast microstructure (Fig. 6B(c-d)). Furthermore, a lamellar eutectic mixture of α-Mg and β-phase surrounded the β-phase precipitates (Fig. 6B(e,f)) [127].

Kubelka et al. [129] studied the microstructure properties of pure Mg matrix SF, reinforced with Al_2O_3–SiO_2-mullite hollow spheres. These foams were manufactured using a pressure-assisted infiltration technique, followed by cooling under three distinct conditions: quenching after complete infiltration (quenching cooling condition (QCC)), cooling in the casting machine (machine cooling condition (MCC)), and additional heat treatment after MCC (heat-treated condition (HTC): normalizing at 500 °C for 120 min). The study revealed that the foam exhibited favorable infiltration behavior, and a reaction zone at the particle-matrix interface was evident irrespective of the cooling condition. The dimensions and composition of the reaction zone exhibited variability depending on the applied conditions (Fig. 7A and B) [129], with quenched samples revealing the most slender reaction zone. This zone consisted of a depleted layer within the hollow sphere and an interface layer containing Mg, Al, Si, and O. The depleted zone exhibited an increase in Mg content and a decrease in Al, Si, and O concentrations, indicating reactions between molten Mg and the depleted alumina and silica of the spheres, resulting in the formation of new phases on the interface, specifically Mg_2Si and MgO. Higher reactivity was observed in MCC and HTC conditions (Fig. 7A). The study also revealed that the depletion zone thickness increased with higher temperatures and holding times, leading to a higher fraction of Al, Si, and O in the Mg matrix [129].

Hollow carbon and activated carbon particles serve as reinforcements for fabricating Mg and Mg-MSFs. Activated carbon is widely utilized for various medical applications, including the oral removal of drug poisoning and gastrointestinal lavage, facilitating the elimination of toxins [137,138]. Therefore, Mg-based foams with both open and closed pore structures have been manufactured using AC particles as porosity agents through MIT [45,128]. In a study, Ferri et al. [128] employed a gas pressure infiltration technique to introduce molten Mg into preforms of hollow spherical carbon particles. Subsequently, the carbon particles were removed via oxidizing heat treatment, resulting in the production of Mg foams characterized by an open pore structure. Microstructure analysis of the foams revealed an average pore size ranging from 450 to 600 μm. It was also observed that the Mg foam underwent oxidation during the heat treatment aimed at eliminating the carbon spheres, leading to the formation of a MgO layer on the surface with an average thickness of 3 μm [128]. In a comparable investigation, Movahedi et al. [45] employed an established counter-gravity infiltration process to fabricate AZ91 SF reinforced with granular and porous AC particles featuring a close-pore structure (Fig. 7C(a)). The microstructural examination of an as-cast AZ91 strut (Fig. 7C(b)) revealed its composition, comprising an α-matrix (95.14 at.% Mg, 4.64 at.% Al, 0.21 at.% Zn, and 0.01 at.% Mn), β-$Mg_{17}Al_{12}$ phase (71.53 at.% Mg, 27.08 at.% Al, 1.37 at.% Zn, and 0.02 at.% Mn), and a eutectic α + β phase. Some Mg-rich areas also contained Al–Mn phases [45]. Additionally, the study demonstrated the intactness of the AC particles, with no observable mechanical damage. It was demonstrated that no reactions took place between the matrix and filler particles. However, despite a protective argon atmosphere, partial matrix oxidation was detected.

Defouw et al. [139] utilized the pressure infiltration method to fabricate SFs, with densities ranging from 0.7 to 1.03 g/cc, with a matrix of either pure Mg or AZ91–Mg alloy reinforced with carbon microspheres. Microstructural analysis of the samples revealed varying quantities of filled spheres and observed porosity attributed to incomplete infiltration. In liquid metallurgy techniques, such as SCTs and MITs, the reactivity between the Mg matrix and common hollow reinforcements like SiO_2, fly ash, and Al_2O_3 often results in the formation

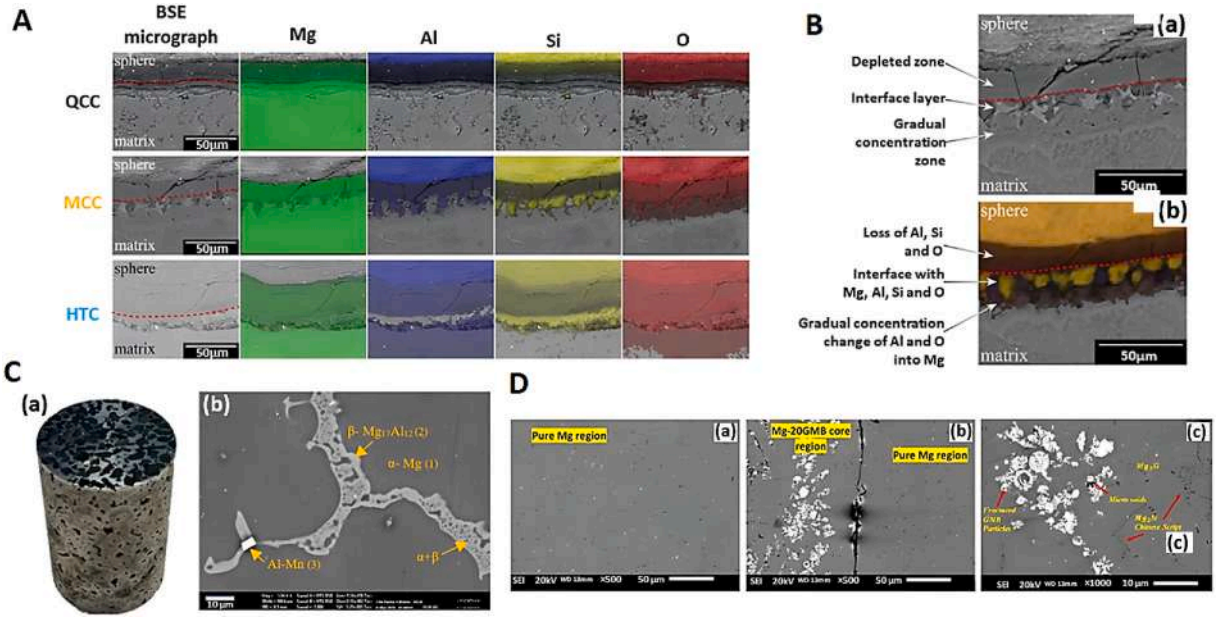

Fig. 7. (A) Energy dispersive X-ray (EDX) mappings of the interfaces in the SFs under three material conditions: QCC, MCC, and HTC, illustrating the presence of the elements Mg, Al, Si, and O. The interface is highlighted with a red dotted line in the backscattered electrons (BSE) images, (B) (a) BSE image of a specimen in the MCC, showcasing the depletion zone, interface layer, and the adjacent gradually changing concentration zone on the interface, as indicated in (b) through a mapping overlay of the elements Al (blue), Si (yellow), and O (red) to visualize the layers and zones [129], (C) (a) Macrostructure of the AZ91–AC SF; and (b) Microstructure of an as-cast AZ91 strut [45], and (D) SEM images of as-cast: (**a**) Monolithic Mg, (**b**) Mg/Mg-20 wt%GMB hybrid, and (c) Mg-20 wt%GMB core material with higher magnification [76]. (For interpretation of the references to color in this figure legend, the reader is referred to the Web version of this article.)

of new phases in the microstructure. These new phases may have detrimental effects, leading to the breakage of reinforcement shells and Mg penetration. However, by implementing specific processing conditions, these adverse effects can be mitigated, and the reaction between the Mg matrix and reinforcement particles can also promote better bonding, improving the mechanical characteristics of the resulting SF [126]. Sankaranarayanan et al. [113] employed the P/M technique, incorporating hybrid MWS, to fabricate Mg-MSFs. The foams were reinforced with FAC particles in varying weight percentages (5–15 wt %). Microstructural examination of the samples revealed uniformly distributed intact cenosphere particles, with a few instances of breakage, showcasing robust interfacial integrity. Additionally, phase analysis of the specimens demonstrated finely distributed intermetallic phases, like MgO and Mg_2Si, formed due to the reaction between the Mg matrix and the FACs.

Matli et al. [76] used P/M and hot extrusion to generate a composite of Mg-20 wt% GMB and monolithic Mg (Fig. 7D(a)). Molten Mg from the CSC technique was disi9ntegrated by DMD and directed onto the core material to make the shell. This produced a hybrid Mg/Mg-20 wt% GMB composite. Microstructural investigation showed a cohesive metallurgical contact between the monolithic Mg shell and the Mg-20 wt% GMB core material (Fig. 7D(b)). The EDX experiment established Mg_2Si as the secondary phase in Mg-20 wt% GMB core material. Micro-voids and fractured GMB particles were also observed (Fig. 7D(c) [76]). In a separate study, lightweight AZ61/FAC SFs were successfully synthesized using P/M and MWS techniques [132]. Microstructural characterizations of the SFs indicated that the FACs were intact, largely undamaged, and uniformly distributed in the matrix. Additionally, MWS proved effective in minimizing the formation of interfacial reaction products in AZ61/FAC SFs. Moreover, a significant weight reduction of approximately 23% was achieved by incorporating FACs into the AZ61 matrix [132]. Based on the findings from the reviewed papers, it becomes evident that predicting the microstructural properties and interfacial reactions between fillers and the matrix in Mg-MSFs, often comprised of hollow particles with various trace elements, poses a considerable challenge.

Microstructure evaluation of fabricated Mg-MSFs utilizing methods based on stir casting demonstrated these fabrication techniques are effective in homogeneous dispersion of fillers in the Mg-based matrix with no fillers cluster formation. However, the main drawbacks of these techniques are the flotation of low-density filler particles and filler particle fracture, which can be seen in several studies due to severe chemical reactions between filler particles and molten Mg-based matrix [72,79,84,123]. The microstructural properties reviewed in this section showed what intermetallic phases are formed according to the reaction between the Mg-based matrix and filler particle shell. Furthermore, it was indicated that these phases' content depends on the elemental composition of the Mg-based alloy matrix and fillers, the fabrication technique, and fabrication parameters. The formation of intermetallic phases between the Mg-based matrix and fillers is essential for the integrity of the Mg-MSFs and vital bonding between the matrix and fillers. Considering the effectiveness of these phases and their amount on the mechanical properties and corrosion behavior of samples, further investigations are needed to provide a broader perspective on the formation of the possible phases in the target Mg-MSFs and to achieve the optimum fabrication parameters to control the formation and amounts of these phases, to achieve the expected properties in the target Mg-MSF.

4.2. Mechanical properties

As mentioned, MMSFs can be classified as various MFs characterized by a close-pore structure. The primary objective in fabricating MMSFs is to attain superior mechanical and EA properties while maintaining a lower density compared to bulk metals. Various parameters influence the density and mechanical properties of MMSFs. These can be managed, including the thickness-to-diameter ratio of reinforcement shell walls, the combination of matrix alloy and hollow particles, processing parameters, thermal treatment, porosity, volume fraction of fillers, and the volume fraction of voids that are formed due to microporosities in the fillers shell [47,140–142]. Additionally, it is worth noting that achieving a homogeneous distribution of particles is crucial in metal matrix composites, particularly in SFs. The heterogeneous distribution of reinforcement can negatively impact the physical and mechanical properties of the composites [114,143–145]. The ability to modify the thermal and mechanical characteristics of SFs by choosing the material, hollow particle volume percentage, and hollow particle wall thickness promotes fast usage expansion. Achieving a balance between high compressive properties and low density is a critical objective in designing MMSFs. Their general stress-strain response under compression has been assessed. The findings indicated a three-part stress-strain behavior: 1) quasi-elastic behavior up to yield stress, 2) a nearly flat plateau region, and 3) densification of MMSF. This response is advantageous for absorbing energy at low stress and is significantly influenced by the hollow particles' properties. When metallic particles are employed, there is a minor transition between the elastic and plateau phases. Conversely, a rapid progression between these phases is observed when the particles' chemical composition is primarily ceramic. While MMSFs generally exhibit lower densities than their matrix metals' bulk form, their densities are notably higher than MFs (with interconnected porosities) made from the same metal as their matrix [146–149]. Despite this, Mg-matrix SFs stand out due to their remarkable mechanical properties, including high EA, low density, high specific strength, and notable biocompatibility. These make them more appealing than other MMSFs, especially for orthopedic applications [150–152]. In the case of MMSFs, energy absorption (EA) refers to the capability of fabricated MMSFs, including Mg-based SFs, to absorb and dissipate energy when subjected to external forces such as compressive or tensile forces. The parameters of density and mechanical properties of MMSFs described earlier are also effective in EA properties. In addition, the rate of applying the external force is also essential in determining EA properties [153–155]. The hardness specifications of MMSFs have a notable influence on their strength, elastic modulus, wear resistance, and manufacturability. The MMSF's ability to withstand mechanical loads is ensured by its suitable hardness qualities tailored to the specific application requirements. The ability of MMSF to absorb energy upon impact or compression is determined by its hardness. When utilizing MgMSFs in biomedical applications, achieving an appropriate level of hardness is crucial. This guarantees that the MgMSF can endure mechanical pressures while facilitating bone formation and integration [156]. In the case of fabricated MgMSFs, microhardness testing is mainly conducted on the fabricated samples' flat and polished surfaces. Since the distribution of hollow particles in the Mg-based SFs may not be completely homogeneous, the microhardness test is usually conducted in different areas of the samples' surfaces where the samples can be in various diameters and shapes (including cylindrical and cuboidal) to attain accurate hardness value [65,73,76,79,133].

The exceptional compressive properties, coupled with an elastic modulus resembling natural bone, position Mg/GMB SFs as a promising option for implant materials [79]. In this regard, Anbuchezhiyan et al. [73] assessed the compressive and hardness properties of AZ91D MgMSF, reinforced with HGM, fabricated by the SC technique. This research demonstrated an increase in the hardness of SFs with higher mass fractions of HGM in the matrix. Furthermore, hardness testing indicated that the presence of reinforcements with higher strength imposes limitations on the plastic deformation of the matrix. However, the extent of constraint on plastic deformation was found to be contingent on the distribution of reinforcement particles in the matrix. In another research [79], mechanical evaluation of pure Mg SFs reinforced with 5%, 15%, and 25% wt% of GMB, fabricated by the DMD technique, revealed that as the GMB content increases, not only does the foam density decrease, but the CTE of the SFs also decreases. This suggests an improvement in dimensional stability for the developed foams.

Furthermore, the study illustrated a consistent increase in the hardness of monolithic Mg with the incremental addition of GMB particles. Regarding compressive properties, the 0.2% compressive yield strength (CYS) and compressive fracture strain of monolithic Mg showed an increase with the addition of GMB. Additionally, the EA during compression also exhibited an augmentation with the progressive addition of GMB [79]. The exceptional compressive properties, coupled with an elastic modulus resembling natural bone, position Mg/GMB SFs as a promising option for implant materials. In a related study, Matli et al. [76] examined the mechanical characteristics of as-cast pure Mg and a hybrid composite, Mg/Mg-20 wt%GMB, manufactured by P/M (blending, compaction, and hot extrusion) and DMD. Compared to pure Mg, the hybrid Mg/Mg-20 wt%GMB composite demonstrated higher 0.2% CYS (↑71.6%), lessened UCS (↓23.25%), and higher ductility (↑186.48%). Fractography analysis showed rough fracture surfaces and shear bands in as-cast Mg (Fig. 8A(a)). Mg/Mg-20 wt%GMB sample fracture modes include matrix fracture and GMB pullout (Fig. 8A(b)). The as-cast Mg/Mg-20 wt%GMB hybrid composite had a rougher surface than pure Mg specimens (Fig. 8A(b)) [76]. Padnuru Sripathy et al. [133] made SFs with Mg as the matrix and 5–20 wt% lightweight GMBs as reinforcement particles. The P/M method and hybrid MWS were used for synthesis. The inclusion of 5, 10, and 20 wt% GMB hollow particles produced Mg-MSFs with 8%, 16%, and 26% lower densities than monolithic Mg [133]. The generated Mg-MSFs similarly increased in hardness with GMB content. GMB hollow particles reduced yield strength, whereas Mg-MSFs improved UCS, fracture strain, and EA capacity. The Mg-5 wt.%GMB composite had the maximum UCS at 321 MPa, 26% greater than monolithic Mg. The fractography of Mg-20 wt% GMB showed interior cracks (Fig. 8B), indicating that the shattered GMB particles could not carry the load, causing samples to fail at lower UCS values. However, the Mg-20 wt%GMB composite outperformed pure Mg by 39% and 65% in fracture strain and EA [133]. In 2018, Anbuchezhiyan et al. [134] investigated the mechanical characteristics of AZ91D alloy reinforced with hollow glass microspheres (HGM) fabricated by a vacuum die-casting process. They examined the impact of various process parameters, including particle size (45 μm, 55 μm, and 65 μm), mass fraction (10%, 15%, and 20%), and stirring speed (450 rpm, 500 rpm, and 600 rpm), on the mechanical characteristics like hardness, compressive strength, porosity, and density of the SFs. Their findings indicated that the optimal process parameters were a particle size of 45 μm, a mass fraction of 20%, and a stirring speed of 600 rpm. Furthermore, it was revealed that particle size had a more significant effect on

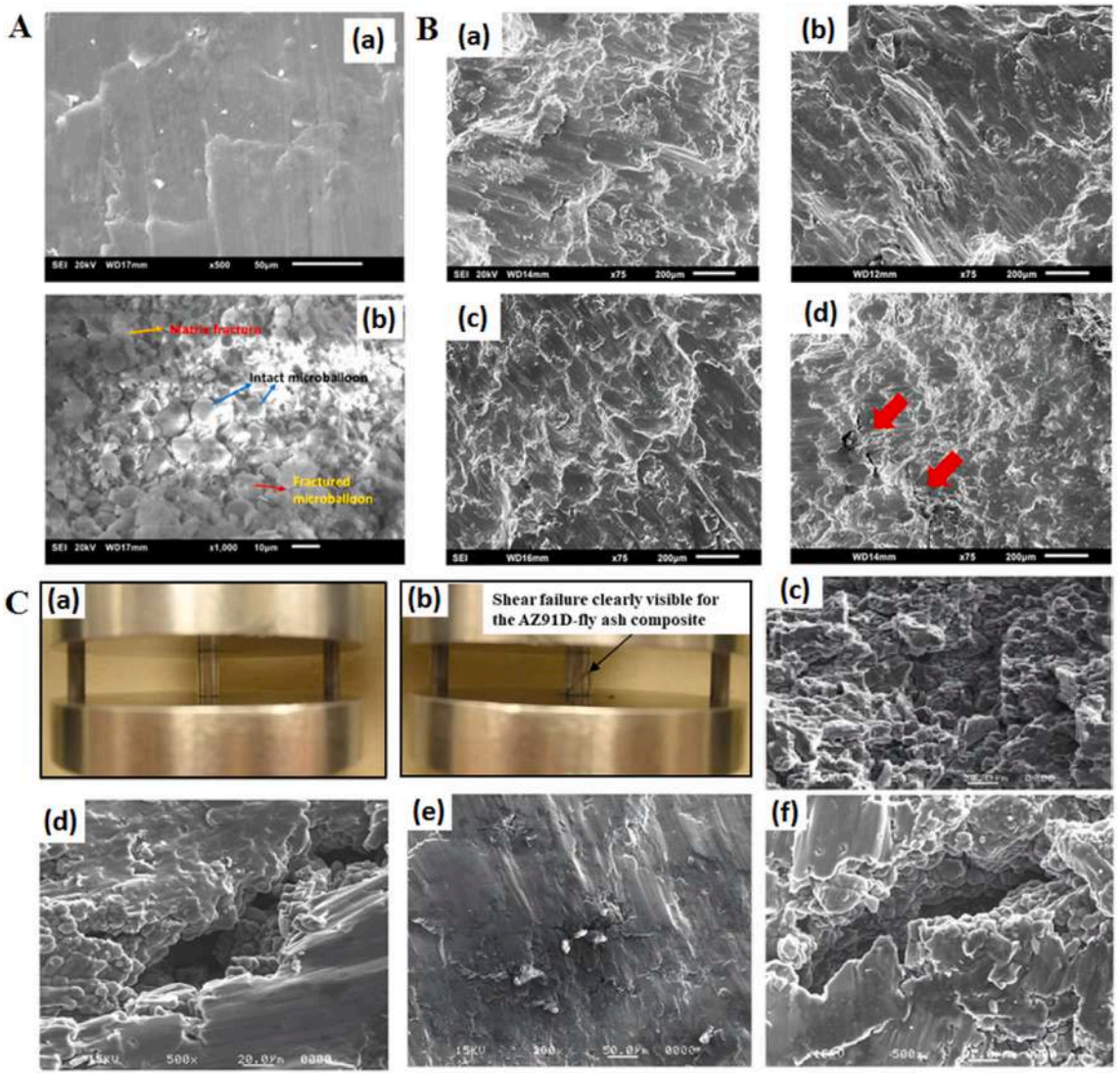

Fig. 8. (A) Fractography analysis of as-cast (a) pure Mg, and (b) Mg/Mg-20 wt%GMB hybrid composite [76], (B) fractography of (**a**) pure Mg, (**b**) Mg-5 wt.%GMB, (**c**) Mg-10 wt%GMB, and (**d**) Mg-20 wt%GMB with arrows showing internal cracks [133], (C) Photographs of the compression sample of AZ91D-5 wt.% FAC composite before (a) and after test showing shear fracture at 45° (b), SEM fractographs of the base matrix AZ91D alloy (c), AZ91D-5 wt.% FAC (d), AZ91D-10 wt% FAC (e), and AZ91D-15 wt% FAC (f) [65].

determining the mechanical properties of the SF due to its important role in determining porosity. Additionally, the study revealed a decrease in the density of the SF with an increase in the mass percentage of hollow glass microspheres [134]. The physical and mechanical characteristics of syntactic foams are largely determined by their porosity. The purpose of the voids is to lower the density of syntactic foams. The compressive materials fill up the matrix porosity under compression. The porosity of the HGM particle is seen upon breakage. Compressing substance can also occupy this porosity. Therefore, the overall porosity of the material structure determines the length of the plateau stress in the stress-strain curve of syntactic foam. Additionally, their findings demonstrated that the enhanced porosity of the HGM particles in the matrix alloy greatly decreased the density of the syntactic foams.

As previously mentioned, FACs are among the most frequently used hollow reinforcements in the fabrication of Mg-based SFs. In this regard, Rohatgi et al. [65] fabricated AZ91D Mg-based SFs (composite) reinforced with 5, 10, and 15 wt% of FACs using the die casting technique (the same as the CSC technique). The study revealed a decrease in sample density as the percentage of FACs increased. The addition of FACs led to an increase in the UTS of the samples. The tensile strength of the AZ91D-5 wt.% FACs SF showed a peak and then decreased for the samples containing 10 and 15 wt% FACs. In addition, Young's modulus of samples decreased with an increasing percentage of FACs in the samples. FACs' fracture and debonding were the main damage features on the samples' fracture surface. When 5 wt% FACs were added to the AZ91D alloy, the UCS and CYS of the SFs went down. Increasing the FAC content to 10 and 15 wt% did not greatly affect the samples' compressive and yield strengths. The composite's failure under compression (Fig. 8C) began with crack formation within the AZ91D matrix due to typical void nucleation and growth. The cracks avoided FACs, favoring propagation through the matrix, leading to the AZ91D-FAC SF fracture [65].

In the case of utilizing Al_2O_3 particles as reinforcement, Mg-MSFs containing Al_2O_3 particles were manufactured using a non-isothermal infiltration casting process, employing a preheated die filled through gas pressure [85]. Analysis of the compressive stress-strain deformation of the SFs revealed significant potential for applications requiring kinetic energy absorption, physical density, and compressive strength. The experimental findings demonstrated that through this technique allows MgMSFs to be tailored for diverse load-bearing and EA requirements. Specifically, achieving a low relative wall thickness in combination with a low matrix strength is essential for EA applications to minimize undesirable stress peaks before reaching the plateau stress. The results also emphasized that when compressive strength is the primary design parameter, alloys with high matrix strength and hollow spheres with thicker walls offer the most significant potential [85].

In another investigation, the compressive properties of an amorphous Mg matrix reinforced with ductile iron spheres were examined [124]. An essential aspect observed in the compressive behavior of the foams is a distinct reduction in flow stress after reaching the yield point. Additionally, it was demonstrated that the iron spheres played a significantly more minor role in the overall load-bearing capacity compared to the matrix. In summary, introducing a network of ductile iron spheres substantially enhanced the compressive failure strain and EA of the amorphous $Mg_{60}Cu_{21}Ag_7Gd_{12}$ alloy. In another study, Rivero et al. [125] conducted experiments on the quasistatic compressive properties of SF consisting of Mg-AZ91 reinforced with about 50 vol% hollow SiC spheres. Their foams were produced employing a sub-atmospheric pressure infiltration process. The study investigated the impact of the AZ91 Mg-based matrix strength on the foam's behavior under high strain rate conditions. Their outcomes demonstrated that the foams' peak strength, plateau strength, and toughness increased proportionally with the yield stress of the matrix material. The evaluation of high strain rate properties in the Mg-AZ91/SiC foams indicated no observed strain rate sensitivity within the range of 0.001–726/s [125].

Research conducted by Akinwekomi et al. [131] used P/M and rapid MWS techniques to fabricate AZ61-Mg alloy SFs with a hybrid pore structure. The hybrid structure incorporated fly ash hollow microspheres and carbamide granules, aiming to achieve SFs with low density and floatability. The SFs were intended for use as micro-boats and chemical release agents. Two groups of samples were tested to assess the impact of varying the volume fractions of each particle on the mechanical and EA properties of the synthesized SFs. One group had different amounts of fly ash microspheres with constant amount of carbamide granules, while the other had the opposite configuration. The results revealed that, for samples with varying fly-ash microsphere volume fractions, both compressive strength and energy absorption capacity (EAC) increased with the increment of fly ash microspheres. The peak was observed at 30 vol% fly ash microspheres before experiencing a drop in samples containing 40 vol% fly ash microspheres. Furthermore, it was observed that in samples with varying carbamide granule volume fractions, both compressive strength and EAC decreased with the increasing volume fraction of carbamide granules. The SF with a volume ratio of AZ61 to fly ash microspheres of 3:2 and 40 vol% carbamide granules exhibited the lowest density and superior floatability [131]. In evaluating the compressive properties of AZ91-AC particle SFs (with a density of 1.12–1.18 g/cm^3), a consistent trend was observed in the EA of the synthesized AZ91–AC SFs. The deformation mechanism in these specimens involved a brittle fracture mode with the formation of shear bands during the fracture of all specimens [45].

Gibson and Ashby [157] proposed a theoretical model for describing the mechanical response of closed-cell foams. They viewed the closed-cell metal foam as a regular hexagonal cellular structure and developed the general equations for evaluating the plateau stress and Young's modulus during compression loading:

$$\sigma_{pl} / \sigma_{ys} = 0.3\ (\Phi.\ \rho_f / \rho_s)^{3/2} + 0.4\ (1\text{-}\Upsilon)\ (\rho_f / \rho_s) \quad (1)$$

$$E^*/\ Es = \Phi^2\ (\rho_f / \rho_s)^{3/2} + (1\text{-}\Upsilon)\ (\rho_f / \rho_s) \quad (2)$$

where σ_{pl} is the plateau stress of the foam, σ_{ys} is the yield stress of the cell wall material, Υ is the fraction of solid contained in the cell edges, ρ_f is the density of the cell wall material, ρ_s is the Young's modulus of the cell wall material. E^* is the density of foam, E^* is the Young's modulus of the foam and Papadopoulos et al. [158] and Idris et al. [159] calculated the theoretical plateau stress and Young's modulus of closed-cell Al foams by using Gibson's equations and compared with their experimental results. The experimental results agreed with the results based on Gibson's theories.

However, closed-cell metal foams have a different compressive behaviour under dynamic compression. Dannemann and Lankford [160] studied the compressive behaviour of metallic foam under high strain rates. They found that the compressive behavior of closed-cell metal foams is also sensitive to the strain rate. Strain rate strengthening occurs in closed-cell Al foam, especially in the higher density Al foam. This strain rate effect may be related to fluid (air) flow through ruptured cell walls, and it appears to be controlled by cell shape, cell size and distribution, cell wall aspect ratio, and uniformity of wall section profile. This behavior is also observed in other studies [161,162]. Yu et al. [163] studied the tensile properties of closed-cell metallic alloy foam with different relative densities. The deformation behavior of the foam subjected to uniaxial tension differed from compression, where the plateau stress regime was not found in tension. The tensile strength and elastic modulus increased with increasing the relative density of the foam [164], approximately agreeing with the Gibson-Ashby model. The summarized results and remarks regarding the mechanical properties of SFs with varying Mg-based matrices are presented in Table 4.

4.3. Corrosion behavior

While Mg-based alloys possess unique and advantageous features like high strength-to-weight ratios and elastic modulus comparable to cancellous bone, making them potential candidates for various

Table 4
A summary of the mechanical properties of diverse SFs with varying Mg-based matrices and fillers, fabricated through different methods.

Fabrication Method	Matrix/reinforcements	Porosity/density	Compressive/tensile properties [MPa]	Energy Absorption/toughness (J/cm^3)	Microhardness (Hv)	Enhancement mechanism/remarks	Refs.
Stir casting	ZC63	Porosity = 0.1% Theoretical density = 1.87 (g/cm^3) Experimental density = 1.85 (g/cm^3)	CYS = 206 UCS = 293	–	–	- The compressive characteristics of the composite foam alloys are diminished compared to the matrix alloy. This discrepancy can be attributed to the lower strength (Young's modulus) of the fly ash microballoons in contrast to the strength of the matrix alloy (Young's modulus) observed in this specific investigation.	[72]
	ZC63 MMSF with 10 vol% fly ash microballons	Theoretical density = 1.73 (g/cm^3) Experimental density = 1.8 (g/cm^3)	CYS = 156 UCS = 239	Specific energy absorption (SEA) = 19.17 MJ/m^3 (at 10% strain)	–	- The composite specimens with 10% and 20% vol% of microballoons display characteristic behavior akin to an elastoplastic foam. They demonstrate an initial linear elastic range, succeeded by an extensive deformation range at a relatively constant stress level, a phenomenon not observed in the solid ZX63 matrix alloy and composites with 25% vol% of microballoons.	
	ZC63 MMSF with 20 vol% fly ash microballons	Theoretical density = 1.6 (g/cm^3) Experimental density = 1.68 (g/cm^3)	CYS = 157 UCS = 348	SEA = 18.65 MJ/m^3 (at 10% strain)	–		
	ZC63 MMSF with 25 vol% fly ash microballons	Theoretical density = 1.54 (g/cm^3) Experimental density = 1.57 (g/cm^3)	CYS = 208 UCS = 270	–	–		
Sub-atmospheric pressure infiltration	AZ91D-matrix SF reinforced with SiC hollow particles	Density = 1.21 (g/cc)	Compressive peak stress (CPS) = 118.2	–	–	- Substantial variations were observed in the peak strength recorded under high strain rates. However, despite these notable fluctuations, the peak strength remains relatively consistent when assessed over the range of strain rates from 0.001 to 726/s. - The sensitivity to strain rate in the context of the Mg-AZ91–SiC SF - The response of foams is primarily governed by the properties of the matrix and is not notably changed by the presence of SiC hollow spheres within the range of strain rates examined in this study.	[125]
Sub-atmospheric pressure infiltration	AZ91D-matrix SF reinforced with SiC hollow particles (average SiC particles diameter and wall thickness are 2 mm and 130 μm respectively)	Density = 0.972 ± 0.047 (g/cm^3)	Compressive strength (CS) = 22 ± 4	Energy density up to peak stress = 0.7 ± 0.1 (MJ/m^3)	–	- The reduction in density to values below 1 g/cm^3 presents new opportunities for the application of MMSFs in buoyancy-related fields, a sector traditionally dominated by polymer matrix SFs until the findings of this research. - The peak strength and the elastic EA increase with strain rate. - While the AZ91D alloy exhibited plastic deformation during the compressive test before failure, the composite's failure mode is characterized by brittleness. - At elevated strain rates, the SF underwent failure marked by the particle crushing, plastic deformation of the matrix, and the crack propagation along the precipitates within the GBs.	[127]
Sub-atmospheric pressure infiltration	AZ91D MMSF with Al_2O_3 hollow particle size range 0.106–0.212 mm	Density = 2.27 (g/cm^3)	CPS = 342	Toughness = 99	–	- The smallest size reinforcements (0.106–0.212 mm) displayed notably higher strength than those with larger sizes. - The MMSF incorporating the smallest Al_2O_3 hollow spheres (0.106–0.212 mm) demonstrated the most favorable combination of specific peak strength and SEA. - Increasing the hollow sphere wall thickness to diameter (t/d) ratio resulted elevated the foam' peak strength, plateau strength, and toughness. - Foams fabricated with smaller spheres, specifically higher EA per unit weight, exhibited enhanced performance.	[126]
	AZ91D MMSF with Al_2O_3 hollow particle (size range 0.106–0.212 mm)	Density = 2.20 (g/cm^3)	CPS = 325	Toughness = 120	–		
	AZ91D MMSF with Al_2O_3 hollow particle size range 0.106–0.212 mm	Density = 2.15 (g/cm^3)	CPS = 280	Toughness = 106	–		
	AZ91D MMSF with Al_2O_3 hollow particle size range 0.106–0.212 mm	Density = 2.31 (g/cm^3)	CPS = 376	Toughness = 124	–		
	AZ91D MMSF with Al_2O_3 hollow particle size range 0.106–0.212 mm	Density = 2.21 (g/cm^3)	CPS = 332	Toughness = 111	–		

(*continued on next page*)

Table 4 (*continued*)

Fabrication Method	Matrix/reinforcements	Porosity/density	Compressive/tensile properties [MPa]	Energy Absorption/toughness (J/cm^3)	Microhardness (Hv)	Enhancement mechanism/remarks	Refs.
	AZ91D MMSF with Al_2O_3 hollow particle size range 0.212–0.425 mm	Density = 1.59 (g/cm^3)	CPS = 261	Toughness = 85	–		
	AZ91D MMSF with Al_2O_3 hollow particle size range 0.212–0.425 mm	Density = 1.90 (g/cm^3)	CPS = 208	Toughness = 68	–		
	AZ91D MMSF with Al_2O_3 hollow particle size range 0.212–0.425 mm	Density = 1.98 (g/cm^3)	CPS = 199	Toughness = 118	–		
	AZ91D MMSF with Al_2O_3 hollow particle size range 0.212–0.425 mm	Density = 1.91 (g/cm^3)	CPS = 256	Toughness = 72	–		
	AZ91D MMSF with Al_2O_3 hollow particle size range 0.212–0.425 mm	Density = 2.10 (g/cm^3)	CPS = 196	Toughness = 64	–		
	AZ91D MMSF with Al_2O_3 hollow particle size range 0.425–0.500 mm	Density = 1.85 (g/cm^3)	CPS = 241	Toughness = 93	–		
	AZ91D MMSF with Al_2O_3 hollow particle size range 0.425–0.500 mm	Density = 1.82 (g/cm^3)	CPS = 221	Toughness = 89	–		
	AZ91D MMSF with Al_2O_3 hollow particle size range 0.425–0.500 mm	Density = 1.83 (g/cm^3)	CPS = 230	Toughness = 82	–		
	AZ91D MMSF with Al_2O_3 hollow particle size range 0.425–0.500 mm	Density = 1.75 (g/cm^3)	CPS = 168	Toughness = 52	–		
	AZ91D MMSF with Al_2O_3 hollow particle size range 0.425–0.500 mm	Density = 1.83 (g/cm^3)	CPS = 206	Toughness = 64	–		
SC	AZ91D alloy	Experimental density = 1.87 g/cc Theoretical density = 1.81 g/cc	CYS = 143 Compressive ultimate strength (CUS) = 211	–	–	- Adding HGM to the matrix significantly reduced the density of SFs due to the increased mass fraction of reinforcement. - The density of SFs was marginally higher than the theoretical value because of the presence of Mg_2Si in the inter matrix alloy. - The hardness of SF increased as the mass fractions of HGM in the matrix alloy increased. - Increasing the mass percentage of HGM in the matrix alloy resulted in a higher plateau stress. - The composite foam with a higher mass fraction of 23% exhibited increased EA, attributed to a more excellent conversion of absorbed energy into plastic deformation during compression.	[73]
	AZ91D MMSF with 15% HGM particle size = 45 μm	3.1 Experimental density = 1.6 g/cc Theoretical density = 1.56 g/cc	CYS = 143 CUS = 211	–	–		
	AZ91D MMSF with 20% HGM particle size = 45 μm	13.1 Experimental density = 1.5 g/cc Theoretical density = 1.48 g/cc	CYS = 161 CUS = 232	–	–		
	AZ91D MMSF with 23% HGM particle size = 45 μm	34.4 Experimental density = 1.4 g/cc Theoretical density = 1.35 g/cc	CYS = 168 CUS = 243	EA = 32.14 MJ/m^3	–		
P/M + rapid MWS	AZ61 MMSF (with volume fractions of AZ61 to carbamide granules = 3:2, and 20 vol% fly ash microspheres)	Theoretical density = 1.00 (g/cm^3) Sintered density = 0.90 (g/cm^3)	CS = 25 ± 3	EA = 6 ± 2	–	- The SF specimens with 40% carbamide granules revealed significant floatability on water.	[131]
	AZ61 MMSF (with volume fractions of AZ61 to carbamide granules = 3:2, and 30 vol% fly ash microspheres)	Theoretical density = 0.97 (g/cm^3) Sintered density = 0.98 (g/cm^3)	CS = 30.1 ± 0.3	EA = 8.4 ± 0.6	–		
	AZ61 MMSF (with volume fractions of AZ61 to carbamide granules = 3:2, and 40 vol% fly ash microspheres)	Theoretical density = 0.93 (g/cm^3) Sintered density = 1.10 (g/cm^3)	CS = 16.1 ± 0.4	EA = 4 ± 1	–		
	AZ61 MMSF (with volume fractions of AZ61 to fly ash microspheres = 3:2, and 20 vol% carbamide granules)	Theoretical density = 1.01 (g/cm^3)	CS = 29 ± 4	EA = 7.8 ± 0.6	–		

(*continued on next page*)

Table 4 (*continued*)

Fabrication Method	Matrix/reinforcements	Porosity/density	Compressive/tensile properties [MPa]	Energy Absorption/toughness (J/cm^3)	Microhardness (Hv)	Enhancement mechanism/remarks	Refs.
		Sintered density = 1.02 (g/cm^3)					
	AZ61 MMSF (with volume fractions of AZ61 to fly ash microspheres = 3:2, and 30 vol% carbamide granules)	Theoretical density = 0.85 (g/cm^3) Sintered density = 0.90 (g/cm^3)	CS = 23 ± 3	EA = 7 ± 1	–		
	AZ61 MMSF (with volume fractions of AZ61 to fly ash microspheres = 3:2, and 40 vol% carbamide granules)	Theoretical density = 0.82 (g/cm^3) Sintered density = 0.79 (g/cm^3)	CS = 16 ± 2	EA = 4.0 ± 0.4	–		
Sub-atmospheric pressure infiltration	36.01 %Vol. AZ91 MMSF with 58.75 % Vol. AC (particle size = ~2.8 mm) Voids volume fraction = 5.24%	Density = 1.12 (g/cm^3)	CPS = 32.45	EA = 9.53 (MJ/m^3)	–	- The specimen's void fraction exhibited a decrease in correlation with density. - The volumetric EA generally increased with density.	[45]
	36.51 %Vol. AZ91 MMSF with 58.75 % Vol. AC (particle size = ~2.8 mm) Voids volume fraction = 4.75%	Density = 1.13 (g/cm^3)	CPS = 40.90	EA = 7.61 (MJ/m^3)	–	- The deformation behavior of the produced AZ91–AC SFs revealed brittle deformation behavior along with some signs of barreling under quasi-static compression.	
	36.92 %Vol. AZ91 MMSF with 58.75 % Vol. AC (particle size = ~2.8 mm) Voids volume fraction = 4.33%	Density = 1.14 (g/cm^3)	CPS = 39.30	EA = 7.85 (MJ/m^3)	–	- The compressive evaluation of the samples indicated a consistent trend for the EA of the fabricated AZ91-AC SFs.	
	37.32 %Vol. AZ91 MMSF with 58.75 % Vol. AC (particle size = ~2.8 mm) Voids volume fraction = 3.93%	Density = 1.15 (g/cm^3)	CPS = 48	EA = 8.30 (MJ/m^3)	–		
	39.38 %Vol. AZ91 MMSF with 58.75 % Vol. AC (particle size = ~2.8 mm) Voids volume fraction = 1.87%	Density = 1.18 (g/cm^3)	CPS = 51.43	EA = 13.49 (MJ/m^3)	–		
DMD	Pure Mg foam	2.1 vol% Density = 1.701 ± 0.002 (g/cc)	0.2% CYS = 66 ± 4 UCS = 194 ± 8	EA = 21 ± 1(MJ/m^3)	47 ± 2	- Foam density decreases with increasing GMB content. - The obtained experimental density values were lower than the corresponding theoretical values.	[79]
	Mg-MSF with 5 vol % GMB	0.72 vol% Density = 1.674 ± 0.015 (g/cc)	0.2% CYS = 77 ± 3 UCS = 232 ± 7	EA = 28 ± 1 (MJ/m^3)	82 ± 4	- The CTE of SFs decreases with the increasing GMB loading. - The progressive addition of GMB particles resulted in a steady increase in the hardness of monolithic Mg.	
	Mg-MSF with 15 vol % GMB	1.78 vol% Density = 1.559 ± 0.010 (g/cc)	0.2% CYS = 102 ± 5 UCS = 231 ± 6	EA = 33 ± 2 (MJ/m^3)	91 ± 5	- Mg-25 wt%GMB foam exhibited the highest amounts of 0.2% CYS and compressive fracture strain, which were ~161 MPa and ~37.7%, respectively.	
	Mg-MSF with 25 vol % GMB	1.98 vol% Density = 1.472 ± 0.018 (g/cc)	0.2% CYS = 161 ± 4 UCS = 216 ± 6	EA = 63 ± 3 (MJ/m^3)	107 ± 6	- The maximum UCS was observed in Mg-5wt.%GMB SF. - Mg-25 wt% foam showing a significant improvement in EA (~200%) as compared to pure Mg.	
DMD followed by hot extrusion	Pure Mg foam	Theoretical density = 1.738 (g/cc) Experimental density = 1.7361 ± 0.0004 (g/cc)	0.2 Tensile yield strength (TYS) = 115 ± 5 Ultimate tensile strength (UTS) = 170 ± 8 Tensile elongation (TE) = 7 ± 1 (%) 0.2% CYS = 70 ± 4 UCS = 180 ± 9 Total compressive strain (TCS) = 16 ± 1 (%)	EA = 19 ± 1 (MJ/m^3)	47 ± 2	- Incorporating fly ash particulates led to a remarkable decrease in density (23%). - The theoretical densities were higher than the experimental densities because of the fly ash particulates fragmentation and their infiltration by the molten Mg. - The microhardness, EA, and compressive properties of the specimens directly correlate with the amount of fly ash particles. - SFs composed of Mg-5 wt.% fly ash exhibited the maximum values for 0.2%TYS and UTS. However, an escalation in the fly ash concentration beyond 5 wt-% instigated a progressive decline in the mechanical strengths (0.2%TYS and UTS) of the composite foams. Despite this reduction, these strengths remained superior to those observed in pure Mg.	[63]
	Mg-MSF including 5 wt% FACs	Theoretical density = 1.5204 (g/cc) Experimental	0.2 TYS = 180 ± 7 UTS = 230 ± 10 TE = 5 ± 1 (%) 0.2% CYS = 100 ± 8	EA = 65 ± 4 (MJ/m^3)	98 ± 2		

(*continued on next page*)

Table 4 (*continued*)

Fabrication Method	Matrix/reinforcements	Porosity/density	Compressive/tensile properties [MPa]	Energy Absorption/toughness (J/cm^3)	Microhardness (Hv)	Enhancement mechanism/remarks	Refs.
		density = 1.6406 ± 0.0048 (g/cc)	UCS = 330 ± 7 TCS = 22 ± 2(%)				
	Mg-MSF including 10 wt% FACs	Theoretical density = 1.3512 (g/cc) Experimental density = 1.4905 ± 0.0085 (g/cc)	0.2 TYS = 150 ± 8 UTS = 215 ± 9 TE = 3 ± 1 (%) 0.2% CYS = 130 ± 12 UCS = 350 ± 6 TCS = 23 ± 2(%)	EA = 70 ± 6 (MJ/m^3)	110 ± 6		
	Mg-MSF including 15 wt% FACs	Theoretical density = 1.2160 (g/cc) Experimental density = 1.4203 ± 0.0136 (g/cc)	0.2 TYS = 130 ± 7 UTS = 180 ± 8 TE = 2 ± 1 (%) 0.2% CYS = 150 ± 4 UCS = 370 ± 6 TCS = 23 ± 2 (%)	EA = 73 ± 3 (MJ/m^3)	112 ± 7		
P/M + DMD	As-cast pure Mg	1.50 % Density = 1.712 ± 0.009 (g/cc)	CYS = 88 ± 3 UCS = 215 ± 5	EA = 36 ± 2 (MJ/m^3)	Shell region = 44 ± 5	The hybrid Mg/Mg-20 wt% GMB composite showed much higher CYS (↑71.6%), lower UCS (↓23.25%), improved ductility (↑186.48%), and lower density than as-cast pure Mg.	[76]
	As-cast Mg/Mg-20 wt% GMB hybrid composite	1.73 % Density = 1.651 ± 0.013 (g/cc)	CYS = 151 ± 4 UCS = 165 ± 3	EA = 51 ± 2 (MJ/m^3)	Shell region = 53 ± 3 Core region = 80 ± 4 Interface region = 74 ± 6		
Vacuum die casting	AZ91D matrix reinforced with 10% mass fraction of HGM (particle size = 45 μm, stirring speed = 450 rpm)	3.78 vol% Density = 1.62 (g/cc)	CS = 241	–	80.9	- The density of syntactic foam decreases with increases in the mass percentage of hollow glass microspheres. - The particle size can provide a higher significant nature among input parameters for the fabrication of magnesium metal matrix composite owing to its ability to determine performance measures - The stirring speed ensures the homogeneous distribution of reinforcement in the matrix alloy - The particle size and mass fraction of reinforcement particles in the matrix of syntactic foams determine the performance measures such as density, compressive strength, porosity, and hardness.	[134]
	AZ91D matrix reinforced with 15% mass fraction of HGM (particle size = 45 μm, stirring speed = 500 rpm)	19 vol% Density = 1.51 (g/cc)	CS = 266	–	119.0		
	AZ91D matrix reinforced with 20% mass fraction of HGM (particle size = 45 μm, stirring speed = 600 rpm)	28 vol% Density = 1.42 (g/cc)	CS = 280	–	148.3		
	AZ91D matrix reinforced with 10% mass fraction of HGM (particle size = 55 μm, stirring speed = 500 rpm)	4.12 vol% Density = 1.58 (g/cc)	CS = 239	–	75.8		
	AZ91D matrix reinforced with 15% mass fraction of HGM (particle size = 55 μm, stirring speed = 600 rpm)	18 vol% Density = 1.48 (g/cc)	CS = 259	–	106		
	AZ91D matrix reinforced with 20% mass fraction of HGM (particle size = 55 μm, stirring speed = 450 rpm)	24 vol% Density = 1.38 (g/cc)	CS = 243	–	116.9		
	AZ91D matrix reinforced with 10% mass fraction of HGM (particle size = 65 μm, stirring speed = 600 rpm)	5.49 vol% Density = 1.56 (g/cc)	CS = 160	–	74.6		
	AZ91D matrix reinforced with 15% mass fraction of HGM (particle size = 65 μm, stirring speed = 450 rpm)	17.2 vol% Density = 1.52 (g/cc)	CS = 211	–	101.3		
	AZ91D matrix reinforced with 20% mass fraction of HGM (particle size = 65 μm, stirring speed = 500 rpm)	22.02 vol% Density = 1.39 (g/cc)	CS = 232	–	114.1		
DMD	Pure Mg	–	0.2 TYS = 103 ± 5 UTS = 148 ± 6 Tensile fracture	–	59 ± 1	- The stepwise addition of hollow silica nanospheres steadily increased the hardness value of pure Mg.	[120]

(*continued on next page*)

Table 4 (*continued*)

Fabrication Method	Matrix/reinforcements	Porosity/density	Compressive/tensile properties [MPa]	Energy Absorption/toughness (J/cm^3)	Microhardness (Hv)	Enhancement mechanism/remarks	Refs.
			strain (TFS) = 7.9 ± 0.5 (%)			- The gradual incorporation of hollow silica nanospheres into Mg improved both 0.2% TYS and UTS, while the tensile failure strain demonstrated a declining trend.	
	Mg-0.5 vol% SiO_2	–	0.2 TYS = 133 ± 3 UTS = 181 ± 1 TFS = 6.7 ± 0.2 (%)	–	73 ± 2		
		Mg-1.0 vol% SiO_2	–	0.2 TYS = 145 ± 2 UTS = 198 ± 7 TFS = 5.7 ± 0.2 (%)	–		
		83 ± 2					
		Mg-1.5 vol% SiO_2	–	0.2 TYS = 152 ± 1 UTS = 203 ± 3 TFS = 5.2 ± 0.2 (%)	–		
89 ± 1							
Mg-2vol% SiO_2	–	0.2 TYS = 167 ± 4 UTS = 217 ± 7 TFS = 4.7 ± 0.3 (%)	–	92 ± 1			
P/M + MWS	Pure Mg	Theoretical Density = 1.74 (g/cc) Experimental density = 1.73 (g/cc)	0.2% CYS = 98 ± 2 UCS = 254 ± 6 Compressive fracture strain (CFS) = 15.8 ± 0.5 (%)	EA = 25 ± 1 (MJ/m^3)	65 1	- Incorporating GMB hollow particles into the Mg matrix resulted in an elevation of its hardness. - The 0.2% CYS and elastic modulus of the synthesized Mg-MSFs decreased with the incorporation of GMB in the Mg matrix. Simultaneously, the UCS of Mg increased with the addition of GMB particles. However, the highest UCS was observed in Mg-5wt.% GMB and further additions of GMB reduced UCS, although it remained higher than that of pure Mg. - The fracture strain of the synthesized Mg-MSFs demonstrated an increase with the inclusion of GMB in the Mg matrix.	[133]
	Mg-5 wt.% GMB	Theoretical Density = 1.59 (g/cc) Experimental density = 1.59 (g/cc)	0.2% CYS = 91 ± 2 UCS = 321 ± 7 CFS = 19.5 ± 0.6 (%)	EA = 39 ± 1 (MJ/m^3)	76 ± 1		
	Mg-10 wt% GMB	Theoretical Density = 1.46 (g/cc) Experimental density = 1.46 (g/cc)	0.2% CYS = 88 ± 1 UCS = 287 ± 6 CFS = 19.6 ± 0.7 (%)	EA = 36 ± 2 (MJ/m^3)	86 ± 1		
	Mg-20 wt% GMB	Theoretical Density = 1.26 (g/cc) Experimental density = 1.28 (g/cc)	0.2% CYS = 85 ± 1 UCS = 280 ± 4 CFS = 22 ± 2 (%)	EA = 41 ± 3 (MJ/m^3)	114 ± 1		
Low-pressure infiltration technique	Mg-G1.45 hollow ceramic spheres (made of 35 wt% Al_2O_3, 45 wt% SiO_2 and 20 wt % mullite)	Density = 1.48–1.51 (g/cm^3)	Average compressive strength (ACS) = 84 ± 2	–	65 ± 8	- The model of Mg matrix syntactic foams showed that fracture in the early stage of compression did not change the strength of the material; however, it significantly lowered the stiffness in the case of Al_2O_3 hollow sphere	[130]
	Mg-G3.83 hollow ceramic spheres (maid of Al_2O_3)	Density = 1.15–1.17 (g/cm^3)	ACS = 59.6 ± 0.7	–	50 ± 5		

applications, including industrial and biomedical uses, their limited corrosion resistance has hindered widespread adoption. The corrosion of Mg alloys occurs when exposed to aggressive solutions or harsh environments because of their low corrosion potential. Similar to other metals, corrosion in Mg-based alloys can be categorized into uniform (or general) and localized (such as pitting) forms of corrosion based on electrochemical, compositional, and microstructural perspectives on a macroscale [165–167]. Metallurgical factors, such as chemical composition, grain size and shapes, size, shape, and distribution of secondary phases or intermetallic compound particles, inclusions, solute-aggregated GBs, crystallographic orientations, and dislocation density, play a fundamental role in determining the form of corrosion [168–170]. It is important to note that pitting corrosion is considered the predominant type of corrosion for Mg-based alloys among various corrosion modes. Furthermore, post-processing treatments, such as extrusion and rolling, along with post-processing heat treatments (e.g., T4, T5, and T6), significantly influence the corrosion mechanism. These treatments can bring about noticeable alterations in microstructure and stress. An essential determinant of the corrosion behavior in Mg-based material systems within an aqueous environment is the chemical composition of the environment, its concentration (especially chloride ion content), and the pH level. Research has indicated that localized corrosion is more likely to occur under low pH values, corresponding to acidic and neutral solutions [171–174]. Fig. 9a illustrates an optical image of the Mg scaffolds along with the corrosion mechanisms of the scaffolds containing micro scale porosity. The Mg-based alloy dissolves as the anode at the beginning of *in vitro* immersion. At the same time, hydrogen is generated via a cathodic reaction, which leads to local alkaline conditions. The formation of a magnesium-hydroxide $Mg(OH)_2$ film on the Mg surface works as a barrier film to prevent more corrosion attacks. Nevertheless, $Mg(OH)_2$ forms a loose layer and can be converted into soluble $MgCl_2$. Over time, this protective hydroxide layer ruptures [165]. At the same time, CO_3^{2-} and PO_4^{3-} are formed on the surface of Mg-based alloy scaffolds. Afterward, a Ca–P based coating is established because the passive film creates sites for its nucleation and growth, using Ca^{2+} and PO_4^{3-} ions from the surrounding solution. The formation of less soluble degradation products causes a decline in the degradation rate of the scaffolds. Further continuation of soaking leads to an equilibrium between the generation and dissolution of corrosion products.

Equation (1) [175] simplifies the corrosion process for Mg-based alloys in a corrosive environment. As per this equation, the primary corrosion products of Mg-based alloys include Magnesium-hydroxide and hydrogen gas. However, it's crucial to recognize that the corrosion of Mg alloys is a complex phenomenon affected by various factors, as mentioned earlier, including the alloy composition, microstructure, and environmental conditions [175]. Notably, in the Mg-based composite, the second phase or fillers function as cathodic sites when the composite is subjected to a corrosive solution. In contrast, the Mg-based matrix exhibits anodic action, as shown in Fig. 9b [176]. As a result, the matrix experiences preferential corrosion, creating isolated pits that eventually get deeper. The anodic reaction forms the pit and releases Mg^{2+} ions that spread outward from the metal surface. To preserve electro-neutrality, chloride ions move inward within the pit. The pit widens and gets bigger as corrosion progresses, undermining the Mg matrix's partially protective layer. Concurrently, a film of MgO/$Mg(OH)_2$ forms a barrier, which is thought to regulate the corrosion effectiveness. However, this film is partially protective and may become damaged, particularly when Cl ions are involved [176].

Equation (1).

i) Anodic reaction (oxidation): $Mg\ (s) \rightarrow Mg^{2+}(aq) + 2e^{-}$
ii) Cathodic reaction (reduction): $2H_2O + 2e^{-} \rightarrow H_2\ (g) + 2OH^{-}\ (aq)$
iii) The overall corrosion reaction: $Mg\ (s) + 2H_2O\ (l) \rightarrow Mg^{2+}(aq) + 2OH^{-}\ (aq) + H_2\ (g)$
iv) Formation of magnesium hydroxide ($Mg(OH)_2$): $Mg^{2+}(aq) + 2OH^{-}\ (aq) \rightarrow Mg(OH)_2\ (s)$ [175].

The low corrosion resistance of Mg-based alloys results in the rapid degradation of mechanical properties over a short period, which can be especially problematic when mechanical performance is critical, such as using Mg-based biomaterials for bone implant applications in load-bearing sites. Various techniques, including alloying [177,178] surface treatment and applying different coatings [179–181], have been employed to improve the corrosion resistance of Mg-based alloys. Regarding the corrosion behavior of MgMSFs, two perspectives can be considered [182–186]. One considers the matrix voids formed due to porosities in the reinforcement shell and are mainly located in the interaction areas between the matrix and reinforcement. The other one considers the potential difference between the metal matrix and reinforcements, arising from differences in matrix and reinforcement materials. The corrosion rate of MgMSFs might be higher than monolithic Mg with a similar structure. On the contrary, the incorporation of reinforcement particles reduces the surface area of the Mg-matrix exposed to the corrosive environment, reducing the corrosion rate [187–192]. Qureshi et al. [121] investigated the corrosion behavior of MgMSFs reinforced with different amounts of HSNS (0.5–2.0 vol%) fabricated through the DMD technique in two simulated body fluids (SBF) electrolytes: phosphate-buffered saline (PBS) and Hank's balanced salt solution (HBSS). They compared the corrosion properties of these samples with pure Mg samples fabricated using the same DMD technique. Results revealed that the addition of HSNS reinforcement to the Mg-matrix resulted in an improvement in the corrosion resistance. Moreover, Mg-1.5 vol% HSNS exhibited the best overall composition, providing consistent results superior to pure Mg in both electrolytes. It is

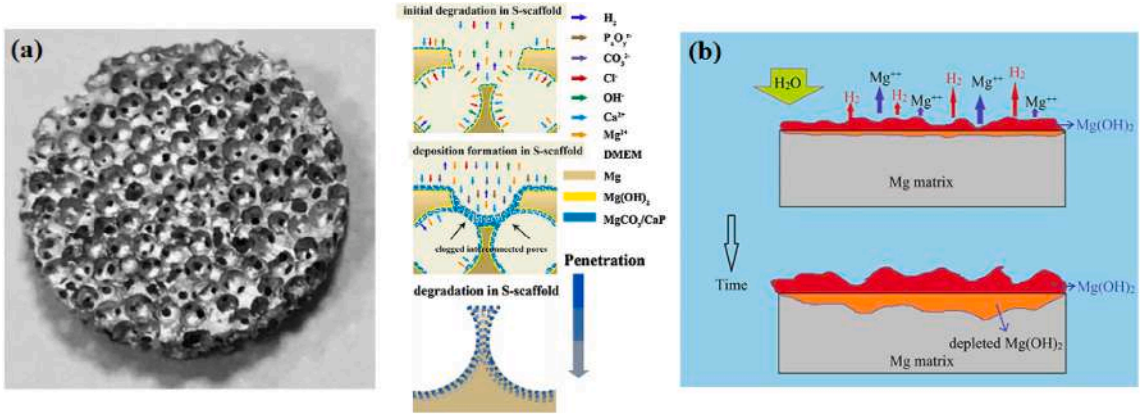

Fig. 9. (a) Optical image of the Mg scaffolds along with schematic illustration of the deposition and the degradation mechanism of the Mg scaffolds [165], and (b) Illustration showing the corrosion mechanism of Mg-based composite [176].

worth noting that each solution affected the samples differently, primarily attributed to the varying composition of the SBFs. In a similar study, Manakari et al. [120] assessed the *in vitro* corrosion behavior of pure Mg, Mg-0.5 vol% GMB and Mg-1.0 vol% GMB SFs, targeting potential use as temporary bone implant materials across four different SBFs: artificial blood plasma solution (ABPS, pH = 7.4), PBS (pH = 7.4), Hank's Balanced Salt Solution (HBSS, pH = 7.4), and artificial saliva solution (ASS, pH = 6.2). Results indicated that the corrosion resistance of Mg-HSNS SFs increased with decreasing chloride, sulfate, and dihydrogen phosphate concentrations, along with an increase in carbonate concentration. Additionally, as shown in Fig. 10A, Mg-1.0 vol% HSNS SF exhibited the best overall corrosion response (except for ABPS), with its corrosion susceptibility ranked in the following order concerning corrosion rate and polarization curves in different SBF solutions: ABPS > PBS > HBSS > ASS. In the ABPS medium, while a protective layer with few pits was observed on the surface of pure Mg, the presence of HSNS reduced the occurrence of pitting in the SFs and aided in the formation of an apatite layer (Fig. 10B) [120]. Notably, in comparison to the pure Mg sample, the passive layer formed on the surface of Mg-1.0 vol% HSNS in ABPS and ASS media exhibited higher density and greater uniformity (Fig. 10B(b,c),C). Additionally, the density of this passive layer was even more pronounced when using the HBSS medium compared to the ASS medium for Mg-1.0 vol% HSNS [120].

Manakari et al. [80] assessed the potential benefits of incorporating HGMB particles to address delamination wear, a typical limitation affecting the competitive advantages of Mg in safety-critical components for bio-implantations. In this investigation, Mg-(15 and 25 wt%) GMB SFs were produced using the DMD technique, and the friction and wear behavior of the samples were examined under dry sliding conditions. The results revealed a reduction in the wear rate of pure Mg with an increase in GMB content (Fig. 11A(a)). The Mg-25 wt%GMB specimen exhibited the lowest wear rate of 0.273 mm^3/N-km, approximately 2.5 times lower than pure Mg (Fig. 11A(a)). Regarding friction, the study demonstrated a decrease in the coefficient of friction (μ) (Fig. 11A(b)) with an increase in GMB content (Fig. 11A(b)) [80]. Mg-25 wt% GMB exhibited a roughly 13% lower μ compared to pure Mg. These findings highlighted the effectiveness of uniformly dispersed GMB particles in significantly enhancing the wear resistance of SFs. As stated, this improvement is crucial for overcoming delamination wear. This factor has traditionally restricted the advantages of composites with discontinuous reinforcements under sliding wear conditions, particularly in structural and biomedical applications [80].

Prasadh et al. [122] investigated the corrosion performance of Mg-MSFs containing hollow SiO_2 nanoparticles at 0.5, 1, and 1.5 vol%, with 10–20 nm particle sizes. They employed a DMD technique to fabricate their Mg-MSFs. This study assessed the developed Mg-MSFs' suitability as potential biodegradable implants for orthopedic and maxillofacial applications in Hank's Balanced Salt Solution (HBSS). The outcomes showed that over 24 h, there was a significant increase in pH values for all samples, reaching 9.2 to 9.4, indicating the interaction of Mg and Mg-based materials with physiological environments (Fig. 11B (b)). This interaction was particularly noticeable in the initial 12–24 h, as shown in Fig. 11B(b). SEM analysis revealed that the presence of SiO_2 nanoparticles contributed to a reduction in pitting extent due to their

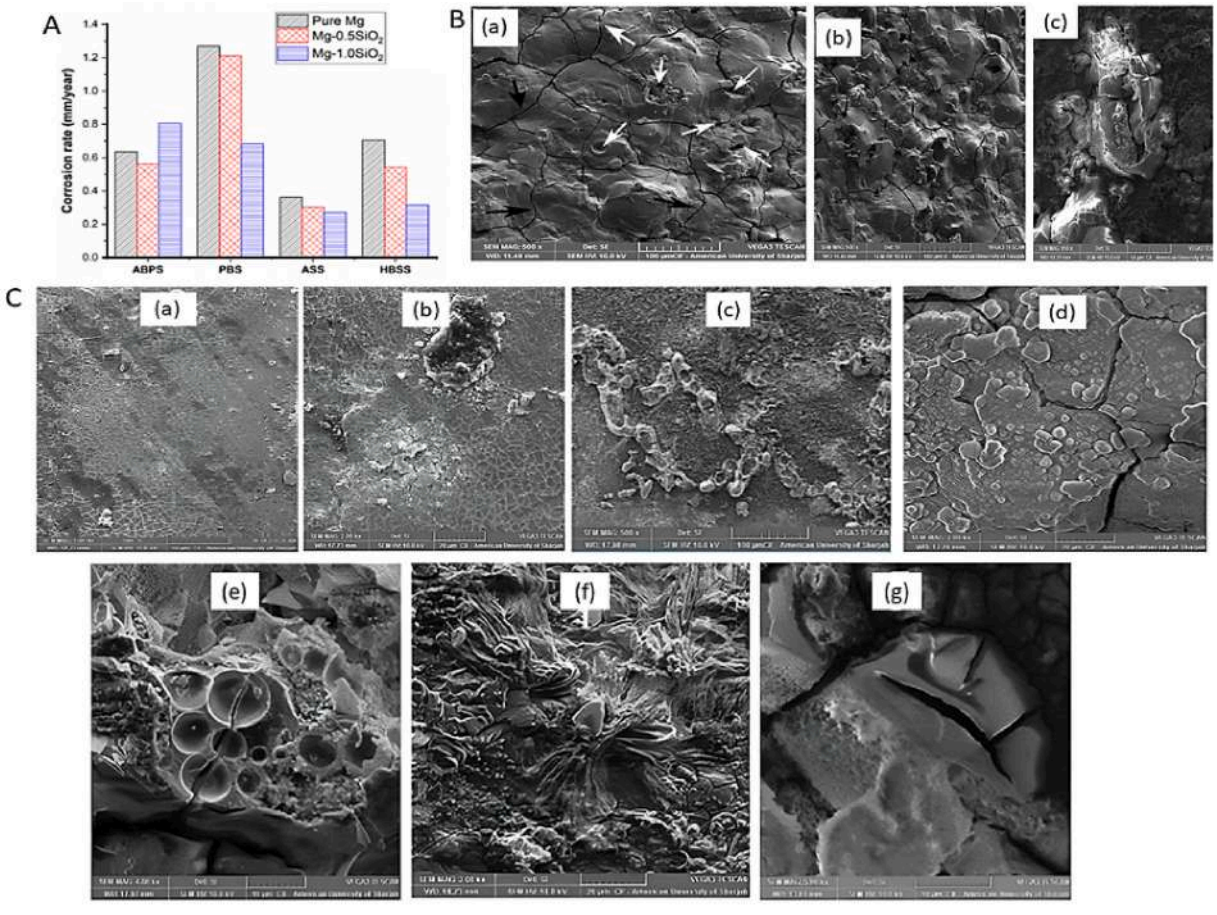

Fig. 10. A: Annual corrosion rate of Mg-HSNS SFs, B: Representative micrographs of corroded surfaces, where (a) shows pure Mg (cross-linked cracks on the surface due to dehydration during SEM sample preparation are indicated) and (b) depicts Mg-1.0 vol%HSNS in ABPS medium, C: Micrographs illustrating corrosion surface morphology, with (a,b) representing pure Mg in ASS and (c–g) showing Mg-1.0 vol% HSNS in ASS at different areas of the sample and various magnifications [120].

near-uniform distribution in the matrix and the resulting decrease in grain size (Fig. 11C). Also, results indicated that the number of pits observed in Mg-1.5 vol% SiO_2 was relatively higher than that of Mg-0.5 vol% SiO_2 and Mg-1.0 vol% SiO_2. Furthermore, it was observed that a more uniformly formed passive layer in the nanocomposites acts as a barrier between the matrix material and the surrounding medium. This delayed the onset of corrosion and reduced the pH compared to pure Mg. Mg-0.5 vol% SiO_2 and Mg-1.0 vol% SiO_2 specimens exhibited a more uniformly formed layer in comparison to Mg-1.5 vol% SiO_2 (Fig. 11C) [122]. The corrosion rates for all samples progressively decreased, except for Mg-1.5 vol% SiO_2 nanocomposite, which showed a slight initial increase. Among the composite specimens, Mg-0.5 vol% SiO_2 nanocomposite displayed the minimum and the most uniformly decreasing corrosion rate, while Mg-1.0 vol% SiO_2 and Mg-1.5 vol% SiO_2 nanocomposites exhibited slightly higher corrosion rates without a consistently uniform trend [122].

The corrosion performance of AZ91D Mg-MSF, reinforced with hollow glass microspheres (HGM), was assessed using the ASTM B117-11 salt spray test [73]. Findings revealed that the base Mg alloy exhibited higher corrosion susceptibility when compared to the Mg alloy reinforced with HGM. The Mg-MSF comprised an α-Mg phase, precipitated β-$Mg_{17}Al_{12}$ phase, and HGM reinforcement phase. It was demonstrated that introducing HGM particles reduced the α-Mg phase, subsequently lowering the corrosion rate of the Mg-MSF. Akinwekomi et al. [131] chose carbamide granules as open-cell formers instead of sodium chloride (NaCl). The primary reason for this substitution was carbamide granules' benign effect on Mg's corrosion during the dissolution stage. In contrast, using NaCl space holders has been reported to exacerbate the corrosion of Mg-based foams. The corrosion behavior of SFs composed of AZ61 Mg alloy and FACs with a diameter of 100–250 μm and a density of 0.70 g/cm3, fabricated through a combination of P/M and MWS techniques, was assessed by Akinwekomi et al. [132]. The outcomes of electrochemical analysis in a sodium chloride solution indicated a shift in Tafel polarization curves towards lower current densities with an increase in the volume fraction of FAC in the SFs. This observation suggests that FACs, under the absence of galvanic interaction between the microspheres and AZ61 matrix, generally enhance the corrosion resistance of the alloy [132]. Table 5 summarizes the results/remarks related to the corrosion properties of SFs with different Mg-based matrixes under various processes.

Research on the Mg and Mg-MSFs' corrosion properties is generally lacking. Considering the significant

potential of Mg-based SFs, conducting additional studies is crucial to expand our understanding of their corrosion behavior. This knowledge is essential for their effective utilization in various industrial and biomedical applications.

5. Conclusions and future directions

Syntactic foams are a novel type of foams that have isolated pore structures. These foams have low densities comparable to metallic and polymeric foams with interconnected pore structures. Additionally, they exhibit superior mechanical and energy absorption properties compared to metallic foams with interconnected pore structures. This makes syntactic foams highly desirable for applications where having both low density and good mechanical properties is crucial. One area of research that stands out is in biomedical applications, which has led to the need for advanced biodegradable materials. Syntactic foams can also be used to construct floating objects, thanks to their lower density than water and impressive mechanical properties. Given their favorable strength-to-density ratio, these materials offer potential applications in various industries, including the automotive industry - where they can enhance car speed and fuel efficiency - and laboratory centrifuge rotors to achieve higher speeds. Therefore, researchers have a growing interest in and appeal to the use of syntactic foams, especially Mg-based ones, due to their low density and adequate biocompatibility, as indicated by the increasing number of publications on this material. The review covers the historical development, current strategies, and potential future

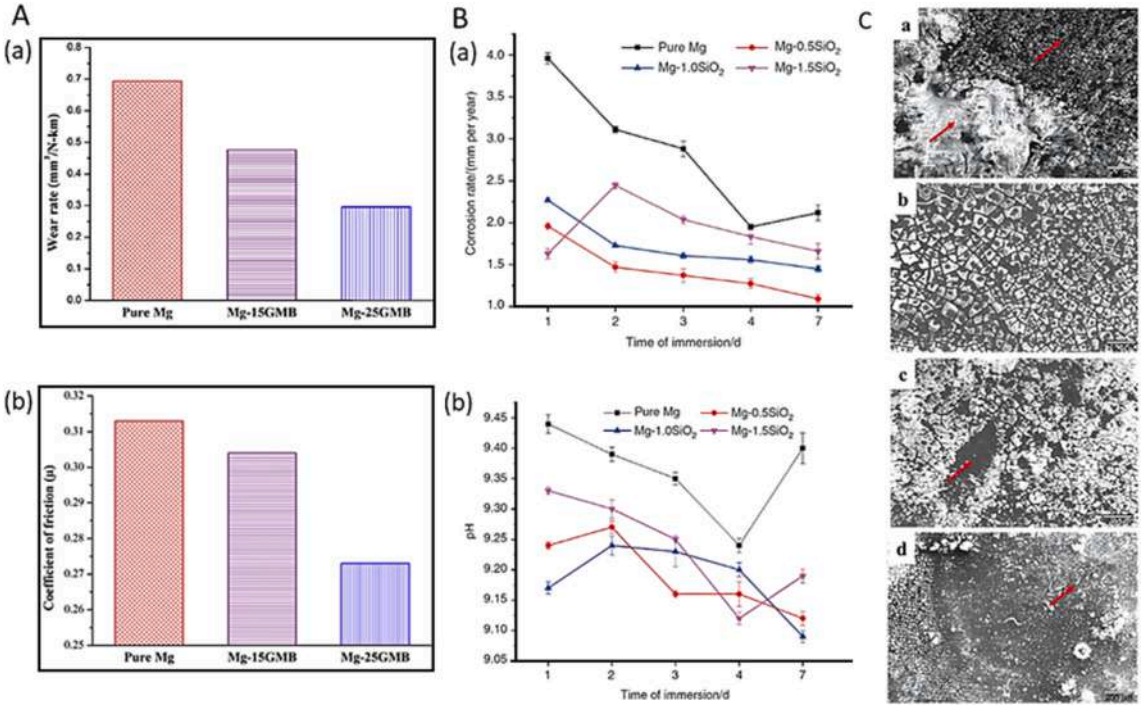

Fig. 11. (A)(a) Wear rates and (b) friction coefficient values for monolithic Mg, Mg-15 wt%GMB, and Mg-25 wt% GMB SFs [80], B: Evaluation of synthesized samples during immersion testing. (a) Corrosion rates, determined through weight loss and (b) pH measurements. (C) SEM images depicting (a) pure Mg, (b) Mg-0.5 vol% SiO2, (c) Mg-1.0 vol% SiO2, and (d) Mg-1.5 vol% SiO2 nanocomposites after 7 days of immersion. Red arrows highlight corroded and non-corroded areas. Magnification, × 75. Scale bars measure 200 μm [122]. (For interpretation of the references to color in this figure legend, the reader is referred to the Web version of this article.)

Table 5
Corrosion properties of different SFs with different Mg-based matrixes and different filler properties, fabricated by various techniques.

Technique	Substrate/ reinforcements	Porosity (%)/pore structure	Electrolyte	Test duration (h)	Ecorr (V/SCE)	icorr (μA/ cm^2)	R_p	Corrosion rate (mm/ year)	Enhancement mechanism/remarks	Ref.
Stir casting	AZ91D (parent alloy)	–	3.5 wt% Salt spray	48	–	–	–	0.032	Adding HGM particles decreased the alpha Mg phase, which reduced the corrosion rate of MMSF.	[73]
	AZ91D matrix with 15% HGM	Close pore structure	3.5 wt% Salt spray	48	–	–	–	0.0074		
	AZ91D matrix with 20% HGM	Close pore structure	3.5 wt% Salt spray	48	–	–	–	0.0017		
	AZ91D matrix with 23% HGM	Close pore structure	3.5 wt% Salt spray	48	–	–	–	0.0013		
DMD	Pure Mg SF	Close pore structure	PBS	–	−1.547 (V)	133.2	41.2 (Ω cm^2)	3.005	- The presence of hollow spheres in Mg-based materials was likely to decrease the Mg content compared to pure Mg for any given vol%. Consequently, the metal matrix's exposure to corrosive environments was reduced. - Hollow spheres within the matrix filled voids and offered sufficient resistance to corrosion, leading to a noticeable improvement in the corrosion rate.	[121]
DMD	Mg matrix with 0.5 vol% HSNS	Close pore structure	PBS	–	−1.551 (V)	46.0	24.4 (Ω cm^2)	1.034		[121]
DMD	Mg matrix with 1.0 vol% HSNS	Close pore structure	PBS	–	−1.563 (V)	6.2	136.4 (Ω cm^2)	0.138		[121]
DMD	Mg matrix with 1.5 vol% HSNS	Close pore structure	PBS	–	−1.553 (V)	46.1	26.4 (Ω cm^2)	1.026		[121]
DMD	Mg matrix with 2.0 vol% HSNS	Close pore structure	PBS	–	−1.542 (V)	390.9	20.4 (Ω cm^2)	8.65		[121]
DMD	Pure Mg SF	Close pore structure	HBSS	–	−1.502 (V)	29.2	265.8 (Ω cm^2)	0.659		[121]
DMD	Mg matrix with 0.5 vol% HSNS	Close pore structure	HBSS	–	−1.488 (V)	19.2	130.1 (Ω cm^2)	0.431		[121]
DMD	Mg matrix with 1.0 vol% HSNS	Close pore structure	HBSS	–	−1.507 (V)	13.6	198.5 (Ω cm^2)	0.304		[121]
DMD	Mg matrix with 1.5 vol% HSNS	Close pore structure	HBSS	–	−1.543 (V)	6.6	238.8 (Ω cm^2)	0.148		[121]
DMD	Mg matrix with 2.0 vol% HSNS	Close pore structure	HBSS	–	−1.522 (V)	2.8	762.8 (Ω cm^2)	0.062		[121]
P/M + MWS	AZ61 matrix	–	3.5% Sodium chloride solution	–	−1462 (mV)	2.86	–	0.071	When the amount of fly-ash microspheres (FAMs) escalated, Tafel polarization curves switched to lower i_{corr}, according to the corrosion performance of syntactic composite foams made of AZ61 and FAMs in solution containing NaCl. This showed that because FAMs reduced the surface area of the specimens subjected to the corrosion environment and reduced galvanic contact, usually diminish the foams' corrosion rate.	[132]
P/M + MWS	AZ61 matrix with 20 vol% fly ash microspheres	23.18 Close pore structure	3.5% Sodium chloride solution	–	−1479 (mV)	2.79	–	0.090		[132]
P/M + MWS	AZ61 matrix with 30 vol% fly ash microspheres	17.83 Close pore structure	3.5% Sodium chloride solution	–	−1413 (mV)	1.83	–	0.055		[132]
P/M + MWS	AZ61 matrix with 40 vol% fly ash microspheres	20.28 Close pore structure	3.5% Sodium chloride solution	–	−1172 (mV)	0.48	–	0.015		[132]
DMD	Pure Mg	Close pore structure	ABPS (pH = 7.4)	–	−1.53	27.77	–	–	- Among the materials tested, monolithic Mg demonstrated the lowest corrosion potential. - The presence of HSNS leads to significant grain refinement, which enables more easily passivating the surface of SFs by breaking down the secondary phase particles along the GB and subsequently improving their corrosion performance. - Materials synthesized under pH 7.4 conditions in APBS, PBS, and HBSS exhibit a higher corrosion rate compared to those in ASS with a pH of 6.2. - The accelerated dissolution process in Mg-1.0 vol% HSNS SF	[120]
DMD	Mg-0.5 vol% HSNS (particle size = 10–20 nm)	Close pore structure	ABPS (pH = 7.4)	–	−1.52	24.45	–	–		[120]
DMD	Mg-1.0 vol% HSNS (particle size = 10–20 nm)	Close pore structure	ABPS (pH = 7.4)	–	−1.48	35.05	–	–		[120]
DMD	Pure Mg	Close pore structure	PBS (pH = 7.4)	–	−1.54	55.46	–	–		[120]
DMD	Mg-0.5 vol% HSNS (particle size = 10–20 nm)	Close pore structure	PBS (pH = 7.4)	–	−1.55	52.76	–	–		[120]
DMD	Mg-1.0 vol% HSNS (particle size = 10–20 nm)	Close pore structure	PBS (pH = 7.4)	–	−1.55	29.67	–	–		[120]
DMD	Pure Mg	Close pore structure	ASS (pH = 6.2)	–	−1.72	15.83	–	–		[120]

(*continued on next page*)

Table 5 (*continued*)

Technique	Substrate/ reinforcements	Porosity (%)/pore structure	Electrolyte	Test duration (h)	Ecorr (V/SCE)	icorr (μA/ cm^2)	R_p	Corrosion rate (mm/ year)	Enhancement mechanism/remarks	Ref.
SF (DMD)	Mg-0.5 vol% HSNS (particle size = 10–20 nm)	Close pore structure	ASS (pH = 6.2)	–	−1.66	13.15	–	–	was attributed to a higher concentration of Cl^- and SO_4^{2-} ions in ABPS compared to PBS and HBSS.	[120]
SF (DMD)	Mg-1.0 vol% HSNS (particle size = 10–20 nm)	Close pore structure	ASS (pH = 6.2)	–	−1.65	11.85	–	–	- Highest corrosion rate is related to PBS, which is due to the higher concentration of dihydrogen phosphate	[120]
DMD	Pure Mg	Close pore structure	HBSS (pH = 7.4)	–	−1.52	30.82	–	–	- Compared to other electrolytic solutions.	[120]
DMD	Mg-0.5 vol% HSNS (particle size = 10–20 nm)	Close pore structure	HBSS (pH = 7.4)	–	−1.48	23.61	–	–		[120]
DMD	Mg-1.0 vol% HSNS (particle size = 10–20 nm)	Close pore structure	HBSS (pH = 7.4)	–	−1.50	13.71	–	–		[120]

directions in using Mg-matrix syntactic foams for various applications. It also comprehensively discusses the fabrication techniques of metallic-based syntactic foams including Mg-based ones, and methods based on stir casting, melt infiltration, and powder metallurgy. Further, it specifically evaluates the microstructural specifications, mechanical properties and corrosion resistance of Mg-based syntactic foams that have been fabricated up to now. The characteristics of the generated Mg-based syntactic foams are influenced by the chemical composition of the Mg-based matrix, the chemical and physical specifications of the filler particles shell, the ratio of filler to matrix, the dispersion of fillers in the matrix, and the fabrication technique and its parameters. Achieving uniform filler dispersion in the Mg-based matrix and adequate interaction between the Mg-based matrix and hollow filler particles is essential for formulating an Mg-based syntactic foam with good mechanical properties and gradual corrosion behavior in corrosive environments. The fabrication technique and its parameters significantly affect the properties of the fabricated Mg-based syntactic foams. Due to the use of high temperatures in methods based on stir casting and melt infiltration compared to powder metallurgy technique, not only is the possibility of Mg-based matrix ignition higher but also the reaction between the molten Mg-based matrix and fillers is more severe, which may lead to filler particle shell fracture and being infiltrated by molten Mg or Mg-based alloy. On the other hand, in powder metallurgy, even though the fabrication temperature is lower, applying mechanical pressure can lead to filler particle shell fracture. Therefore, choosing an adequate fabrication technique and its optimum parameters according to the chemical and mechanical properties of Mg-based matrix and fillers and the ratio of filler to matrix is essential for fabricating Mg-based syntactic foam with the desired properties. The formation of the intermetallic phases, their chemical composition, and their amount, which happen due to the reaction between the Mg-based matrix and fillers, can significantly affect the mechanical properties of the fabricated Mg-based syntactic foams and are mainly dependent on the chemical composition of the Mg-based matrix and filler shell, the fabrication technique and its parameters. Adding stiffer and stronger reinforcements enhances the hardness of syntactic Mg-based foam. By adjusting the content of fillers, we can customize the mechanical and degradation characteristics of the Mg-based syntactic foams according to the application's specific requirements. Corrosion evaluation results suggest the chemical composition of the Mg-based matrix and fillers, hollow filler particles shell structure (especially the presence of microvoids), and the percentage of fillers strongly affect the degradation of Mg-based syntactic foams, mainly due to changes in the surface area and reactivity with the corrosive environment. Furthermore, since the majority of fillers present a much lower density due to their inner hollow space compared to the Mg-based matrix, the density of the fabricated Mg-based syntactic foams significantly decreases with an increase in reinforcement mass fraction. Adding stiffer and stronger reinforcements enhances the hardness of syntactic Mg-based foam. In orthopedic applications, especially at load-bearing sites, Mg-based syntactic foams containing biocompatible hollow filler particles can be a potential candidate and demonstrate higher mechanical properties and corrosion resistance than Mg-based foams with interconnected porosities.

Further research is necessary to evaluate the possibility of combining multiple fillers to create MgMSFs with more targeted and specific properties for a given application or attaining novel properties that would not be achievable by utilizing a single filler type. Furthermore, more investigations are vital for enhancing the biocompatibility of MgMSFs for orthopedic applications and improving the biological properties of MgMSFs, such as osteointegration, osteoconductivity, osteoinductivity, and cell viability. In addition, discovering optimized parameters for fabrication techniques to prevent or at least minimize the unwanted reactions between fillers and matrix, which can have a harmful and unpredicted effect on the mechanical properties and corrosion behavior or induce the desired response between reinforcements and the matrix, is essential to achieve MgMSFs with desired specifications. In addition, the possibility of applying various surface modifications, such as different coatings or surface chemical conversion, to enhance the corrosion properties of these foams for applications in corrosive environments for both industrial and biomedical purposes should be investigated. Furthermore, it is suggested that the possibility of loading hollow reinforcements with biological molecules such as growth factors or medicines such as antibiotics to induce and/or improve properties such as cell differentiation, cell proliferation, or antibacterial properties be evaluated, which requires using low temperatures during the fabrication process to prevent the degradation of the loaded pharmaceutical or biological agent.

Declaration of competing interest

The authors declare that they have no known competing financial interests or personal relationships that could have appeared to influence the work reported in this paper.

Abbreviations

ABPS	Artificial blood plasma solution
AC	Activated Carbon
Al	Aluminum
ASS	Artificial saliva solution
ASTM	American Society for Testing and Materials
ZC	Zinc-copper
BSE	Backscattered electrons
CFS	Compressive fracture strain
CMB	Ceramic microballoon
CPS	Compressive peak stress

CS	Compressive strength
CSC	Conventional stir casting
CTE	Coefficient of thermal expansion
CUS	Compressive ultimate strength
CYS	Compressive yield strength
DMD	Disintegrated melt deposition
EA	Energy absorption
EAC	Energy absorption capacity
EDS	Energy dispersive X-ray spectroscopy
EG	Expanded glass
EP	Expanded perlite
FAC	Fly-ash cenosphere
FTIR	Fourier transform infrared spectroscopy
GB	Grain boundaries
GMB	Glass microballoon
HBSS	Hank's Balanced Salt Solution
HCS	Hollow carbon sphere
HGM	Hollow glass microsphere
HGMB	Hollow glass microballoon
HSCS	Hollow silicon carbide spheres
HSNS	Hollow Silica nano-spheres
HTC	Heat-treated condition
MCC	Machine cooling condition
MF	Metallic foam
Mg	Magnesium
Mg-MSF	Magnesium-matrix syntactic foam
MIT	Melt infiltration technique
AZ	Aluminum-zinc
MSF	Metal syntactic foam
MMC	Metal matrix composite
MMSF	Metal matrix syntactic foam
MWS	Microwave sintering
P/M	Powder metallurgy
PBS	Phosphate-buffered saline
PF	Polymeric foam
QCC	Quenching cooling condition
SBF	Simulated body fluid
SC	Stir casting
SCT	Stir casting technique
SEA	Specific energy absorption
SEM	Scanning electron microscope
SF	Syntactic foam
SiC	Sn
Silicon carbide	Tin
SPS	Spark plasma sintering
TCS	Total compressive strain
TE	Tensile elongation
TFS	Tensile fracture strain
Ti	Titanium
TYS	Tensile yield strength
UCS	Ultimate compressive strength
UTS	Ultimate tensile strength
XRD	X-ray diffraction
Zn	Zinc

References

[1] Broxtermann S, Vesenjak M, Krstulović-Opara L, Fiedler T. Quasi static and dynamic compression of zinc syntactic foams. J Alloys Compd 2018;768:962–9.

[2] S.K. Srivastava, G.K. Gupta, T.C. Joshi, D.K. Rajak, S.K.J. Sanskrita, D. Mondal, A. K. Srivastava, Insight into classifications and manufacturing processes of metallic foams: a review, Proc IME E J Process Mech Eng, 09544089231190551.

[3] Peng B, Xu H, Song F, Wen P, Tian Y, Zheng Y. Additive manufacturing of porous magnesium alloys for biodegradable orthopedic implants: process, design, and modification. J Mater Sci Technol 2024;182:79–110.

[4] Yazdimamaghani M, Razavi M, Vashaee D, Moharamzadeh K, Boccaccini AR, Tayebi L. Porous magnesium-based scaffolds for tissue engineering. Mater Sci Eng C 2017;71:1253–66.

[5] Sezer N, Evis Z, Koç M. Additive manufacturing of biodegradable magnesium implants and scaffolds: review of the recent advances and research trends. J Magnesium Alloys 2021;9(2):392–415.

[6] Suamte L, Tirkey A, Barman J, Jayasekhar Babu P. Various manufacturing methods and ideal properties of scaffolds for tissue engineering applications. Smart Materials in Manufacturing 2023;1:100011.

[7] Guillory RJ, Mostaed E, Oliver AA, Morath LM, Earley EJ, Flom KL, Kolesar TM, Mostaed A, Summers HD, Kwesiga MP, Drelich JW, Carlson KD, Dragomir-Daescu D, Goldman J. Improved biocompatibility of Zn–Ag-based stent materials by microstructure refinement. Acta Biomater 2022;145:416–26.

[8] Ardakani MS, Kampe SL, Drelich JW. Flow stress stabilization of Zn-Cu-Mn-Mg alloys using thermomechanical processing. Mater Char 2022;188:111928.

[9] Mirkhalaf M, Men Y, Wang R, No Y, Zreiqat H. Personalized 3D printed bone scaffolds: a review. Acta Biomater 2023;156:110–24.

[10] Mostaed E, Sikora-Jasinska M, Ardakani MS, Mostaed A, Reaney IM, Goldman J, Drelich JW. Towards revealing key factors in mechanical instability of bioabsorbable Zn-based alloys for intended vascular stenting. Acta Biomater 2020;105:319–35.

[11] Ardakani MS, Mostaed E, Sikora-Jasinska M, Kampe SL, Drelich JW. The effects of alloying with Cu and Mn and thermal treatments on the mechanical instability of Zn-0.05Mg alloy. Mater Sci Eng, A 2020;770:138529.

[12] Willbold E, Gu X, Albert D, Kalla K, Bobe K, Brauneis M, Janning C, Nellesen J, Czayka W, Tillmann W, Zheng Y, Witte F. Effect of the addition of low rare earth elements (lanthanum, neodymium, cerium) on the biodegradation and biocompatibility of magnesium. Acta Biomater 2015;11:554–62.

[13] Xu C, Liu Z, Chen X, Gao Y, Wang W, Zhuang X, Zhang H, Dong X. Bone tissue engineering scaffold materials: fundamentals, advances, and challenges. Chin Chem Lett 2024;35(2):109197.

[14] Shuai C, Wang B, Yang Y, Peng S, Gao C. 3D honeycomb nanostructure-encapsulated magnesium alloys with superior corrosion resistance and mechanical properties. Compos B Eng 2019;162:611–20.

[15] Uppal G, Thakur A, Chauhan A, Bala S. Magnesium based implants for functional bone tissue regeneration – a review. J Magnesium Alloys 2022;10(2):356–86.

[16] Kucharczyk A, Naplocha K, Kaczmar JW, Dieringa H, Kainer KU. Current status and recent developments in porous magnesium fabrication. Adv Eng Mater 2018; 20(1):1700562.

[17] Zhao D, Witte F, Lu F, Wang J, Li J, Qin L. Current status on clinical applications of magnesium-based orthopaedic implants: a review from clinical translational perspective. Biomaterials 2017;112:287–302.

[18] Luo Y, Wang J, Ong MTY, Yung PS-h, Wang J, Qin L. Update on the research and development of magnesium-based biodegradable implants and their clinical translation in orthopaedics. Biomaterials Translational 2021;2(3):188.

[19] Wang JL, Xu JK, Hopkins C, Chow DHK, Qin L. Biodegradable magnesium-based implants in orthopedics—a general review and perspectives. Adv Sci 2020;7(8): 1902443.

[20] Bairagi D, Mandal S. A comprehensive review on biocompatible Mg-based alloys as temporary orthopaedic implants: current status, challenges, and future prospects. J Magnesium Alloys 2022;10(3):627–69.

[21] Zhou H, Liang B, Jiang H, Deng Z, Yu K. Magnesium-based biomaterials as emerging agents for bone repair and regeneration: from mechanism to application. J Magnesium Alloys 2021;9(3):779–804.

[22] Kapłon H, Blawert C, Chęcmanowski J, Naplocha K. Development of open-porosity magnesium foam produced by investment casting. J Magnesium Alloys 2022;10(7):1941–56.

[23] Guo X, Wang Q. Magnesium-based biodegradable metal materials: past, present and future. Biomaterials Translational 2021;2(3):175.

[24] Shahin M, Munir K, Wen C, Li Y. Magnesium matrix nanocomposites for orthopedic applications: a review from mechanical, corrosion, and biological perspectives. Acta Biomater 2019;96:1–19.

[25] Espiritu J, Meier M, Seitz J-M. The current performance of biodegradable magnesium-based implants in magnetic resonance imaging: a review. Bioact Mater 2021;6(12):4360–7.

[26] Rajak DK, Gupta M. Applications of metallic foams. In: Rajak DK, Gupta M, editors. An insight into metal based foams: processing, properties and applications. Singapore: Springer Singapore; 2020. p. 21–37.

[27] Kim HJ, Lee K-Y, Shin G-Y, Shim DS. Fabrication of aluminum (AlSi10Mg) matrix particle (Ti and Zr) reinforced composite foam using directed energy deposition. Opt Laser Technol 2023;167:109806.

[28] Nawaz A, Rani S. Fabrication, properties evaluation, and process optimization of aluminium 6063 alloy foam. Can Metall Q 2023:1–16.

[29] Quadbeck P, Jehring U, Böhm H-D, Füssel A, Standke G. Manufacturing process of low-contamination titanium foam as implant material for cranioplasty based on replica technique. Adv Eng Mater 2024:2301392.

[30] Majumdar DD, Sahu S, Mondal DP, Roychowdhury A, Jha AK, Ghosh M. Microstructural analysis and corrosion behavior of a titanium cenosphere composite foam fabricated by powder metallurgy route. ChemistrySelect 2023;8 (12):e202203581.

[31] Sharma VM, Pal SK, Racherla V. Effect of tool traverse speed on fabrication of open-cell copper foam using friction processing. Int J Adv Des Manuf Technol 2021;116(7):2137–47.

[32] Chang C, Chen G, Wu F, Han Z, Pei L. Fabrication and thermal performance of 3D copper-mesh-sintered foam/paraffin phase change materials for solar thermal energy storage. Processes 2022;10(5):897.

[33] Zhang Y-P, Yang J-H, Li L-L, Cui C-X, Li Y, Liu S-Q, Zhou X-M, Qu L-B. Facile fabrication of superhydrophobic copper- foam and electrospinning polystyrene fiber for combinational oil–water separation. Polymers 2019;11(1):97.

[34] Zhang W, Wei S, Tang W, Hua K, Cui C-x, Zhang Y, Zhang Y, Wang Z, Zhang S, Qu L. Fabrication of a superhydrophobic surface using a simple in situ growth method of HKUST-1/copper foam with hexadecanethiol modification. New J Chem 2020;44(17):7065–70.
[35] Kumar N, Bharti A, Prasad D. Analysis of production techniques for metal foams of iron and steel. Powder Metall Met Ceram 2022;61(5):287–97.
[36] Sundarram SS, Jiang W, Li W. Fabrication of small pore-size nickel foams using electroless plating of solid-state foamed immiscible polymer blends. J Manuf Sci Eng 2014;136(2).
[37] Clancy RB, Cochran JK, Sanders TH. Fabrication and properties of hollow sphere nickel foams. MRS Online Proc Libr 1994;372(1):155–63.
[38] Xu Z, Fu J, Luo T, Yang Y. Effects of cell size on quasi-static compressive properties of Mg alloy foams. Mater Des 2012;34:40–4.
[39] Dutta S, Devi KB, Roy M. Processing and degradation behavior of porous magnesium scaffold for biomedical applications. Adv Powder Technol 2017;28 (12):3204–12.
[40] Yuan L, Ding S, Wen C. Additive manufacturing technology for porous metal implant applications and triple minimal surface structures: a review. Bioact Mater 2019;4:56–70.
[41] Gupta N, Zeltmann SE, Shunmugasamy VC, Pinisetty D. Applications of polymer matrix syntactic foams. JOM 2014;66(2):245–54.
[42] Al-Sahlani K, Taherishargh M, Kisi E, Fiedler T. Controlled shrinkage of expanded glass particles in metal syntactic foams. Materials 2017;10(9):1073.
[43] Shunmugasamy VC, Mansoor B, Gupta N. Cellular magnesium matrix foam composites for mechanical damping applications. JOM 2016;68(1):279–87.
[44] Bolat Ç, Bilge G, Gökşenli A. An Investigation on the effect of heat treatment on the compression behavior of aluminum matrix syntactic foam fabricated by sandwich infiltration casting. Mater Res 2021;24.
[45] Movahedi N, Taherishargh M, Belova IV, Murch GE, Fiedler T. Mechanical and microstructural characterization of an AZ91–activated carbon syntactic foam. Materials 2018;12(1):3.
[46] Agbedor S-O, Yang D-h, Cao J, Chen J-q, Saleh B, Qiu C, Wang Et AL L. Recent progress in porous Mg-based foam preparation approaches: effect of processing parameters on structure and mechanical property. J Iron Steel Res Int 2022;29: 371–402.
[47] Gupta N, Luong DD, Cho K. Magnesium matrix composite foams—density, mechanical properties, and applications. Metals 2012;2(3):238–52.
[48] Karunakaran R, Ortgies S, Tamayol A, Bobaru F, Sealy MP. Additive manufacturing of magnesium alloys. Bioact Mater 2020;5(1):44–54.
[49] Jahangir MN, Mamun MAH, Sealy MP. A review of additive manufacturing of magnesium alloys. In: AIP conference proceedings, vol. 1980. AIP Publishing; 2018, 030026.
[50] Bär F, Berger L, Jauer L, Kurtuldu G, Schäublin R, Schleifenbaum JH, Löffler JF. Laser additive manufacturing of biodegradable magnesium alloy WE43: a detailed microstructure analysis. Acta Biomater 2019;98:36–49.
[51] Rohatgi P, Kim J, Gupta N, Alaraj S, Daoud A. Compressive characteristics of A356/fly ash cenosphere composites synthesized by pressure infiltration technique. Compos Appl Sci Manuf 2006;37(3):430–7.
[52] Zanjad N, Pawar S, Nayak C. Use of fly ash cenosphere in the construction Industry: a review. Mater Today Proc 2022;62:2185–90.
[53] Yang Q, Yu B, Hu H, Hu G, Miao Z, Wei Y, Sun W. Melt flow and solidification during infiltration in making steel matrix syntactic foams. Mater Sci Technol 2019;35(15):1831–9.
[54] Chaitanya CS, Rao R. Surface failure of syntactic foams in sliding contact. Mater Today Proc 2019;15:63–7.
[55] Chen J-p, Ma H-h, Wang Y-x, Huang L-l, Shen Z-w. Effect of hydrogen-storage pressure on the detonation characteristics of emulsion explosives sensitized by glass microballoons. Defence Technology 2022;18(5):747–54.
[56] Cai C, Su Q, Huang S, Li F, Jin H, Yu X, Liu Y, Yang Y, Chen Z. Rheological behaviour, setting time, compressive strength and microstructure of mortar incorporating supplementary cementitious materials and nano-silica. RSC Adv 2023;13(25):17264–81.
[57] Xue Y, Liu R, Xie S, Liu R, Jing W, Liu J, Guo A. Alumina hollow sphere-based ceramics bonded with preceramic polymer-filler derived ceramics. Ceram Int 2019;45(2):2612–20.
[58] Wright A, Kennedy A. The processing and properties of syntactic Al foams containing low cost expanded glass particles. Adv Eng Mater 2017;19(11): 1600467.
[59] Al-Sahlani K, Broxtermann S, Lell D, Fiedler T. Effects of particle size on the microstructure and mechanical properties of expanded glass-metal syntactic foams. Mater Sci Eng, A 2018;728:80–7.
[60] Thalmaier G, Sechel NA, Csapai A, Popa CO, Batin G, Gábora A, Mankovits T, Vida-Simiti I. Aluminum perlite syntactic foams. Materials 2022;15(15):5446.
[61] Kemény A, Katona B, Movahedi N, Fiedler T. Fatigue tests of zinc aluminium matrix syntactic foams filled with expanded perlite. In: IOP conference series: materials science and engineering. IOP Publishing; 2020, 012050.
[62] Luong DD, Gupta N, Daoud A, Rohatgi PK. High strain rate compressive characterization of aluminum alloy/fly ash cenosphere composites. JOM 2011; 63:53–6.
[63] Nguyen QB, Sharon Nai M, Nguyen AS, Seetharaman S, Wai Leong E, Gupta M. Synthesis and properties of light weight magnesium–cenosphere composite. Mater Sci Technol 2016;32(9):923–9.
[64] Huang Z, Yu S, Liu J, Zhu X. Microstructure and mechanical properties of in situ Mg_2Si/AZ91D composites through incorporating fly ash cenospheres. Mater Des 2011;32:4714–9.
[65] Rohatgi P, Daoud A, Schultz B, Puri T. Microstructure and mechanical behavior of die casting AZ91D-Fly ash cenosphere composites. Compos Appl Sci Manuf 2009; 40(6–7):883–96.
[66] Sánchez de la Muela AM, Duarte J, Santos Baptista J, García Cambronero LE, Ruiz-Román JM, Elorza FJ. Stir casting routes for processing metal matrix syntactic foams: a scoping review. Processes 2022;10(3):478.
[67] S-de-la-Muela AM, Cambronero LEG, Ruiz-Román JM. Molten metal infiltration methods to process metal matrix syntactic foams. Metals 2020;10(1):149.
[68] Marx J, Rabiei A. Overview of composite metal foams and their properties and performance. Adv Eng Mater 2017;19(11):1600776.
[69] Qin Y, Wen P, Guo H, Xia D, Zheng Y, Jauer L, Poprawe R, Voshage M, Schleifenbaum JH. Additive manufacturing of biodegradable metals: current research status and future perspectives. Acta Biomater 2019;98:3–22.
[70] Li X, Liu X, Wu S, Yeung K, Zheng Y, Chu PK. Design of magnesium alloys with controllable degradation for biomedical implants: from bulk to surface. Acta Biomater 2016;45:2–30.
[71] Li Y, Zhou J, Pavanram P, Leeflang M, Fockaert L, Pouran B, Tümer N, Schröder K-U, Mol J, Weinans H. Additively manufactured biodegradable porous magnesium. Acta Biomater 2018;67:378–92.
[72] Daoud A, Abou El-khair M, Abdel-Aziz M, Rohatgi P. Fabrication, microstructure and compressive behavior of ZC63 Mg–microballoon foam composites. Compos Sci Technol 2007;67(9):1842–53.
[73] Anbuchezhiyan G, Mohan B, Sathianarayanan D, Muthuramalingam T. Synthesis and characterization of hollow glass microspheres reinforced magnesium alloy matrix syntactic foam. J Alloys Compd 2017;719:125–32.
[74] Muhammad F, Jalal S. A comparative study of the impact of the stirrer design in the stir casting route to produce metal matrix composites. Adv Mater Sci Eng 2021;2021:4311743.
[75] Daoud A. Synthesis and characterization of novel ZnAl22 syntactic foam composites via casting. Mater Sci Eng, A 2008;488(1–2):281–95.
[76] Matli PR, Sheng JGY, Parande G, Manakari V, Chua BW, Wong SCK, Gupta M. A new method to lightweight magnesium using syntactic composite core. Appl Sci 2020;10(14):4773.
[77] Gupta M, Parande G, Manakari V. An insight into high performance magnesium alloy/nano-metastable-syntactic composites. In: 17th Australian international aerospace congress: aiac; 2017.
[78] Gupta M, Wong W. Magnesium-based nanocomposites: lightweight materials of the future. Mater Char 2015;105:30–46.
[79] Manakari V, Parande G, Doddamani M, Gupta M. Enhancing the ignition, hardness and compressive response of magnesium by reinforcing with hollow glass microballoons. Materials 2017;10(9):997.
[80] Manakari V, Parande G, Doddamani M, Gupta M. Evaluation of wear resistance of magnesium/glass microballoon syntactic foams for engineering/biomedical applications. Ceram Int 2019;45(7):9302–5.
[81] Ceschini L, Dahle A, Gupta M, Jarfors AEW, Jayalakshmi S, Morri A, Rotundo F, Toschi S, Singh RA. Casting routes for the production of Al and Mg based nanocomposites. In: Ceschini L, Dahle A, Gupta M, Jarfors AEW, Jayalakshmi S, Morri A, Rotundo F, Toschi S, Singh RA, editors. Aluminum and magnesium metal matrix nanocomposites. Singapore: Springer Singapore; 2017. p. 41–93.
[82] Ceschini L, Dahle A, Gupta M, Jarfors AEW, Jayalakshmi S, Morri A, Rotundo F, Toschi S, Singh RA. Ex situ production routes for metal matrix nanocomposites. In: Ceschini L, Dahle A, Gupta M, Jarfors AEW, Jayalakshmi S, Morri A, Rotundo F, Toschi S, Singh RA, editors. Aluminum and magnesium metal matrix nanocomposites. Singapore: Springer Singapore; 2017. p. 19–40.
[83] Kumarasamy SP, Vijayananth K, Thankachan T, Muthukutti GP. Investigations on mechanical and machinability behavior of aluminum/flyash cenosphere/Gr hybrid composites processed through compocasting. J Appl Res Technol 2017;15 (5):430–41.
[84] Huang Z, Yu S. Microstructure characterization on the formation of in situ Mg2Si and MgO reinforcements in AZ91D/Flyash composites. J Alloys Compd 2011;509 (2):311–5.
[85] Hartmann M, Reindel K, Singer R. Fabrication and properties of syntactic magnesium foams, vol. 521. MRS Online Proceedings Library (OPL); 1998. p. 211.
[86] Manakari V, Parande G, Gupta M. Effects of hollow fly-ash particles on the properties of magnesium matrix syntactic foams: a review. Materials Performance and Characterization 2016;5(1):116–31.
[87] Rohatgi PK, Gupta N, Schultz BF, Luong DD. The synthesis, compressive properties, and applications of metal matrix syntactic foams. JOM 2011;63: 36–42.
[88] Broxtermann S, Taherishargh M, Belova I, Murch G, Fiedler T. On the compressive behaviour of high porosity expanded Perlite-Metal Syntactic Foam (P-MSF). J Alloys Compd 2017;691:690–7.
[89] Rao CP, Suresh R. Corrosion and wear studies on LM6 grade aluminum-cenosphere composite–An experimental approach. Mater Today Proc 2018;5(5): 11667–77.
[90] Zhao Y, Tao X, Xue X. Manufacture and mechanical properties of metal matrix syntactic foams. Mater Sci Technol 2008;4:2607–15.
[91] Myers K, Cortes P, Conner B, Wagner T, Hetzel B, Peters K. Structure property relationship of metal matrix syntactic foams manufactured by a binder jet printing process. Addit Manuf 2015;5:54–9.
[92] Bárczy T, Kaptay G. Modeling the infiltration of liquid metals into porous ceramics, Materials Science Forum. Trans Tech Publ; 2004. p. 297–302.
[93] Rohatgi P, Guo R, Iksan H, Borchelt E, Asthana R. Pressure infiltration technique for synthesis of aluminum–fly ash particulate composite. Mater Sci Eng, A 1998; 244(1):22–30.

[94] Trumble K. Spontaneous infiltration of non-cylindrical porosity: close-packed spheres. Acta Mater 1998;46(7):2363–7.
[95] Orbulov IN, Dobránszky J. Producing metal matrix syntactic foams by pressure infiltration, Periodica Polytechnica. Engineering. Mech Eng 2008;52(1):35.
[96] Tekumalla S, Gupta M. An insight into ignition factors and mechanisms of magnesium based materials: a review, Materials & Design, vol. 113; 2017. p. 84–98.
[97] Parande G, Manakari V, Meenashisundaram GK, Gupta M. Enhancing the tensile and ignition response of monolithic magnesium by reinforcing with silica nanoparticulates. J Mater Res 2017;32(11):2169–78.
[98] Balan P, Thiagarajan V, Ganesan SP, Raghunathan V, Shankar KV, Kumar BGY, Ramalingam VV. Characterization of powder metallurgy processed magnesium alloys for biomedical implants. Emergent Materials 2023;6(2):573–81.
[99] Arora GS, Saxena KK, Mohammed KA, Prakash C, Dixit S. Manufacturing techniques for Mg-based metal matrix composite with different reinforcements. Crystals 2022;12(7):945.
[100] Tandon R. An update on magnesium-based powder metallurgy and additive manufacturing processes. In: Maier P, Barela S, Miller VM, Neelameggham NR, editors. Magnesium Technology 2022. Cham: Springer International Publishing; 2022. p. 17–8.
[101] Govindaraju M, Megalingam A, Murugasan J, Vignesh RV, Kota PK, Ram AS, Lakshana P, Kumar VN. Investigations on the tribological behavior of functionally gradient iron-based brake pad material. Proc IME C J Mech Eng Sci 2020;234(12): 2474–86.
[102] Schade C. Blending and premixing of metal powders and binders. 2015.
[103] Singh S, Bhatnagar N. A survey of fabrication and application of metallic foams (1925–2017). J Porous Mater 2018;25:537–54.
[104] Bakhsheshi-Rad H, Hamzah E, Staiger MP, Dias GJ, Hadisi Z, Saheban M, Kashefian M. Drug release, cytocompatibility, bioactivity, and antibacterial activity of doxycycline loaded Mg-Ca-TiO2 composite scaffold. Mater Des 2018; 139:212–21.
[105] Bakhsheshi-Rad HR, Dayaghi E, Ismail AF, Madzlan A, Akhavan-Farid A, Xiongbiao C. Synthesis and in-vitro characterization of biodegradable porous magnesium-based scaffolds containing silver for bone tissue engineering. Trans Nonferrous Metals Soc China 2019;29(5):984–96.
[106] Oriňaková R, Gorejová R, Králová ZO, Petráková M, Oriňak A. Novel trends and recent progress on preparation methods of biodegradable metallic foams for biomedicine: a review. J Mater Sci 2021;56(25):13925–63.
[107] Guo J, Floyd R, Lowum S, Maria J-P, Herisson de Beauvoir T, Seo J-H, Randall CA. Cold sintering: progress, challenges, and future opportunities. Annu Rev Mater Res 2019;49:275–95.
[108] Rahaman MN. Sintering theory and fundamentals. 2015.
[109] Freni P, Tecchio P, Rollino S, De Benedetti B. Porosity characterization of biomedical magnesium foams produced by Spark Plasma Sintering. In: 2014 IEEE international symposium on medical measurements and applications (MeMeA). IEEE; 2014. p. 1–6.
[110] Akinwekomi AD, Choy MT, Law WC, Tang CY. Finite element modelling of CNT-filled magnesium alloy matrix composites under microwave irradiation, Materials Science Forum. Trans Tech Publ; 2016. p. 83–7.
[111] Akinwekomi AD, Law W-C, Tang C-Y, Chen L, Tsui C-P. Rapid microwave sintering of carbon nanotube-filled AZ61 magnesium alloy composites. Compos B Eng 2016;93:302–9.
[112] Batienkov R, Bol'shakova A, Khudnev A. Microwave sintering of metal powder materials. Metallurgist 2022;65(9–10):1163–73.
[113] Sankaranarayanan S, Nguyen Q, Shabadi R, Almajid A, Gupta M. Powder metallurgy hollow fly ash cenospheres' particles reinforced magnesium composites. Powder Metall 2016;59(3):188–96.
[114] Anbuchezhiyan G, Mohan B, Karthikeyan R. Development of magnesium matrix syntactic foams processed through powder metallurgy techniques, Applied Mechanics and Materials. Trans Tech Publ; 2015. p. 281–6.
[115] Sahmani S, Saber-Samandari S, Khandan A, Aghdam MM. Influence of MgO nanoparticles on the mechanical properties of coated hydroxyapatite nanocomposite scaffolds produced via space holder technique: fabrication, characterization and simulation. J Mech Behav Biomed Mater 2019;95:76–88.
[116] Yilong L, Guibao Q, Yang Y, Xuewei L, Chenguang B. Preparation and compressive properties of magnesium foam. Rare Met Mater Eng 2016;45(10): 2498–502.
[117] Dayaghi E, Bakhsheshi-Rad H, Hamzah E, Akhavan-Farid A, Ismail A, Aziz M, Abdolahi E. Magnesium-zinc scaffold loaded with tetracycline for tissue engineering application: in vitro cell biology and antibacterial activity assessment. Mater Sci Eng C 2019;102:53–65.
[118] Brown A, Zaky S, Ray Jr H, Sfeir C. Porous magnesium/PLGA composite scaffolds for enhanced bone regeneration following tooth extraction. Acta Biomater 2015; 11:543–53.
[119] Kannan S, Pervaiz S, Alhourani A, Klassen RJ, Selvam R, Haghshenas M. On the role of hollow aluminium oxide microballoons during machining of AZ31 magnesium syntactic foam. Materials 2020;13(16):3534.
[120] Manakari V, Kannan S, Parande G, Doddamani M, Columbus S, Vincent S, Gupta M. In-vitro degradation of hollow silica reinforced magnesium syntactic foams in different simulated body fluids for biomedical applications. Metals 2020; 10(12):1583.
[121] Qureshi W, Kannan S, Vincent S, Eddine N, Muhammed A, Gupta M, Karthikeyan R, Badari V. Influence of silica nanospheres on corrosion behavior of magnesium matrix syntactic foam. In: IOP conference series: materials science and engineering. IOP Publishing; 2018, 012012.
[122] Prasadh S, Manakari V, Parande G, Wong RCW, Gupta M. Hollow silica reinforced magnesium nanocomposites with enhanced mechanical and biological properties with computational modeling analysis for mandibular reconstruction. Int J Oral Sci 2020;12(1):31.
[123] Liu JA, Yu SR, Huang ZQ, Ma G, Liu Y. Microstructure and compressive property of in situ Mg2Si reinforced Mg-microballoon composites. J Alloys Compd 2012; 537:12–8.
[124] Brothers A, Dunand D, Zheng Q, Xu J. Amorphous Mg-based metal foams with ductile hollow spheres. J Appl Phys 2007;102(2):023508.
[125] Rivero GAR, Schultz BF, Ferguson J, Gupta N, Rohatgi PK. Compressive properties of Al-A206/SiC and Mg-AZ91/SiC syntactic foams. J Mater Res 2013;28(17): 2426–35.
[126] Newsome DB, Schultz BF, Ferguson J, Rohatgi PK. Synthesis and quasi-static compressive properties of Mg-AZ91D-Al2O3 syntactic foams. Materials 2015;8 (9):6085–95.
[127] Anantharaman H, Shunmugasamy VC, Strbik III OM, Gupta N, Cho K. Dynamic properties of silicon carbide hollow particle filled magnesium alloy (AZ91D) matrix syntactic foams. Int J Impact Eng 2015;82:14–24.
[128] Ferri J, Molina J, Louis E. Fabrication of Mg foams for biomedical applications by means of a replica method based upon spherical carbon particles. Biomedical Physics & Engineering Express 2015;1(4):045002.
[129] Kubelka P, Kádár C, Jost N. Effect of the interface on the compressive properties of magnesium syntactic foams. Mater Lett 2021;287:129293.
[130] Kádár C, Kubelka P, Szlancsik A. On the compressive properties of aluminum and magnesium syntactic foams: experiment and simulation. Mater Today Commun 2023;35:106060.
[131] Akinwekomi AD, Tang C-Y, Tsui GC-P, Law W-C, Chen L, Yang X-S, Hamdi M. Synthesis and characterisation of floatable magnesium alloy syntactic foams with hybridised cell morphology. Mater Des 2018;160:591–600.
[132] Akinwekomi AD. Microstructural characterisation and corrosion behaviour of microwave-sintered magnesium alloy AZ61/fly ash microspheres syntactic foams. Heliyon 2019;5(4):e01531.
[133] Padnuru Sripathy A, Handjaja C, Manakari V, Parande G, Gupta M. Development of lightweight magnesium/glass micro balloon syntactic foams using microwave approach with superior thermal and mechanical properties. Metals 2021;11(5): 827.
[134] Anbuchezhiyan G, Muthuramalingam T, Mohan B. Effect of process parameters on mechanical properties of hollow glass microsphere reinforced magnesium alloy syntactic foams under vacuum die casting. Arch Civ Mech Eng 2018;18:1645–50.
[135] Cao S, Ma N, Zhang Y, Bo R, Lu Y. Fabrication, mechanical properties, and multifunctionalities of particle reinforced foams: a review. Thin-Walled Struct 2023;186:110678.
[136] Drelich JW, Goldman J. Bioresorbable vascular metallic scaffolds: current status and research trends. Current Opinion in Biomedical Engineering 2022;24:100411.
[137] Alkhatib AJ, Al Zailaey K. Medical and environmental applications of activated charcoal. Eur Sci J 2015;11(3).
[138] Joshi PB, Chavali M, Tripati GK, Tondwalkar S. Medical applications of activated carbon. In: Verma C, Quraishi MA, editors. Activated carbon: progress and applications. The Royal Society of Chemistry; 2023.
[139] DeFouw JD, Rohatgi PK. Low density magnesium matrix syntactic foams. Supplemental Proceedings: Materials Fabrication, Properties, Characterization, and Modeling 2011;2:797–804.
[140] Gupta N, Rohatgi PK. Metal matrix syntactic foams: processing, microstructure, properties and applications. DEStech Publications, Inc; 2014.
[141] Xing F, Li S, Yin D, Xie J, Rommens PM, Xiang Z, Liu M, Ritz U. Recent progress in Mg-based alloys as a novel bioabsorbable biomaterials for orthopedic applications. J Magnesium Alloys 2022;10(6):1428–56.
[142] Yang J, Guo JL, Mikos AG, He C, Cheng G. Material processing and design of biodegradable metal matrix composites for biomedical applications. Ann Biomed Eng 2018;46:1229–40.
[143] Liu Y, Zheng Y, Chen XH, Yang JA, Pan H, Chen D, Wang L, Zhang J, Zhu D, Wu S. Fundamental theory of biodegradable metals—definition, criteria, and design. Adv Funct Mater 2019;29(18):1805402.
[144] Zeng Z, Salehi M, Kopp A, Xu S, Esmaily M, Birbilis N. Recent progress and perspectives in additive manufacturing of magnesium alloys. J Magnesium Alloys 2022;10(6):1511–41.
[145] Morgenthal I, Andersen O, Kostmann C, Stephani G, Studnitzky T, Witte F, Kieback B. Highly porous magnesium alloy structures and their properties regarding degradable implant application. Adv Eng Mater 2014;16(3):309–18.
[146] Abazari S, Shamsipur A, Bakhsheshi-Rad HR, Drelich JW, Goldman J, Sharif S, Ismail AF, Razzaghi M. Magnesium-based nanocomposites: a review from mechanical, creep and fatigue properties. J Magnesium Alloys 2023;11(8): 2655–87.
[147] Badkoobeh F, Mostaan H, Rafiei M, Bakhsheshi-Rad HR, RamaKrishna S, Chen X. Additive manufacturing of biodegradable magnesium-based materials: design strategies, properties, and biomedical applications. J Magnesium Alloys 2023;11 (3):801–39.
[148] Khorashadizade F, Abazari S, Rajabi M, Bakhsheshi-Rad HR, Ismail AF, Sharif S, Ramakrishna S, Berto F. Overview of magnesium-ceramic composites: mechanical, corrosion and biological properties. J Mater Res Technol 2021;15: 6034–66.
[149] Daroonparvar M, Kay CM, Mat Yajid MA, Bakhsheshi-Rad HR, Razzaghi M. 2 - fundamentals of additive manufacturing of metallic components by cold spray technology. In: Kumar P, Misra M, Menezes PL, editors. Tribology of additively manufactured materials. Elsevier; 2022. p. 39–85.

[150] Singh S, Vashisth P, Shrivastav A, Bhatnagar N. Synthesis and characterization of a novel open cellular Mg-based scaffold for tissue engineering application. J Mech Behav Biomed Mater 2019;94:54–62.
[151] Bonithon R, Kao AP, Fernández MP, Dunlop JN, Blunn GW, Witte F, Tozzi G. Multi-scale mechanical and morphological characterisation of sintered porous magnesium-based scaffolds for bone regeneration in critical-sized defects. Acta Biomater 2021;127:338–52.
[152] Xue J, Singh S, Zhou Y, Perdomo-Pantoja A, Tian Y, Gupta N, Witham TF, Grayson WL, Weihs TP. A biodegradable 3D woven magnesium-based scaffold for orthopedic implants. Biofabrication 2022;14(3):034107.
[153] Costanza G, Tata ME. Parameters affecting energy absorption in metal foams, Materials Science Forum. Trans Tech Publ; 2019. p. 1552–7.
[154] Meng J, Liu T-W, Wang H-Y, Dai L-H. Ultra-high energy absorption high-entropy alloy syntactic foam. Compos B Eng 2021;207:108563.
[155] Zhang B, Wang L, Zhang J, Jiang Y, Wang W, Wu G. Deformation and energy absorption properties of cenosphere/aluminum syntactic foam-filled circular tubes under lateral quasi-static compression. Int J Mech Sci 2021;192:106126.
[156] Kalpakoglou T, Yiatros S. Metal foams: a review for mechanical properties under tensile and shear stress. Frontiers in Materials 2022;9:998673.
[157] Gibson LJ, Ashby MF. Cellular solids: structure and properties. 2 ed. Cambridge: Cambridge University Press; 1997.
[158] Papadopoulos D, Konstantinidis IC, Papanastasiou N, Skolianos S, Lefakis H, Tsipas D. Mechanical properties of Al metal foams. Mater Lett 2004;58(21): 2574–8.
[159] Idris MI, Vodenitcharova T, Hoffman M. Mechanical behaviour and energy absorption of closed-cell aluminium foam panels in uniaxial compression. Mater Sci Eng, A 2009;517(1–2):37–45.
[160] Dannemann KA, Lankford Jr J. High strain rate compression of closed-cell aluminium foams. Mater Sci Eng, A 2000;293(1–2):157–64.
[161] Deshpande V, Fleck N. High strain rate compressive behaviour of aluminium alloy foams. Int J Impact Eng 2000;24(3):277–98.
[162] Mukai T, Kanahashi H, Miyoshi T, Mabuchi M, Nieh T, Higashi K. Experimental study of energy absorption in a close-celled aluminum foam under dynamic loading. Scripta Mater 1999;40(8):921–7.
[163] Yu H-j, Yao G-c, Liu Y-h. Tensile property of Al-Si closed-cell aluminum foam. Trans Nonferrous Metals Soc China 2006;16(6):1335–40.
[164] Zhang Y. Mechanical properties of metal matrix syntactic foam. of Liverpool: University; 2020.
[165] Jia G, Chen C, Zhang J, Wang Y, Yue R, Luthringer-Feyerabend BJ, et al. In vitro degradation behavior of Mg scaffolds with three-dimensional interconnected porous structures for bone tissue engineering. Corrosion Sci 2018;144:301–12.
[166] Asadi J, Korojy B, Hosseini SA, Alishahi M. Effect of cell structure on mechanical and bio-corrosion behavior of biodegradable Mg-Zn-Ca foam. Mater Today Commun 2021;28:102715.
[167] Ma X, Jing Z, Feng C, Qiao M, Xu D. Research and development progress of porous foam-based electrodes in advanced electrochemical energy storage devices: a critical review. Renew Sustain Energy Rev 2023;173:113111.
[168] Bakhsheshi-Rad HR, Dayaghi E, Ismail AF, Aziz M, Akhavan-Farid A, Chen X. Synthesis and in-vitro characterization of biodegradable porous magnesium-based scaffolds containing silver for bone tissue engineering. Trans Nonferrous Metals Soc China 2019;29(5):984–96.
[169] Dayaghi E, Bakhsheshi-Rad HR, Hamzah E, Akhavan-Farid A, Ismail AF, Aziz M, Abdolahi E. Magnesium-zinc scaffold loaded with tetracycline for tissue engineering application: in vitro cell biology and antibacterial activity assessment. Mater Sci Eng C 2019;102:53–65.
[170] Bakhsheshi-Rad HR, Hamzah E, Staiger MP, Dias GJ, Hadisi Z, Saheban M, Kashefian M. Drug release, cytocompatibility, bioactivity, and antibacterial activity of doxycycline loaded Mg-Ca-TiO2 composite scaffold. Mater Des 2018; 139:212–21.
[171] Rong-Chang Z, Zheng-Zheng Y, Xiao-Bo C, Dao-Kui X. Corrosion types of magnesium alloys. In: Tomasz T, Wojciech B, Mariusz K, editors. Magnesium alloys. Rijeka: IntechOpen; 2018. Ch. 3.
[172] Cheng M-q, Wahafu T, Jiang G-f, Liu W, Qiao Y-q, Peng X-c, Cheng T, Zhang X-l, He G, Liu X-y. A novel open-porous magnesium scaffold with controllable microstructures and properties for bone regeneration. Sci Rep 2016;6(1):24134.
[173] Kleer-Reiter N, Julmi S, Feichtner F, Waselau A, Klose C, Wriggers P, Maier H, Meyer-Lindenberg A. Biocompatibility and degradation of the open-pored magnesium scaffolds LAE442 and La2. Biomed Mater 2021;16(3):035037.
[174] Bonithon R, Lupton C, Roldo M, Dunlop JN, Blunn GW, Witte F, Tozzi G. Open-porous magnesium-based scaffolds withstand in vitro corrosion under cyclic loading: a mechanistic study. Bioact Mater 2023;19:406–17.
[175] Zhao S, Tayyebi M, Yarigarravesh Mahdireza, Hu G. A review of magnesium corrosion in bio-applications: mechanism, classification, modeling, in-vitro, and in-vivo experimental testing, and tailoring Mg corrosion rate. J Mater Sci 2023;58 (30):12158–81.
[176] Rashad M, Pan F, Asif M, Chen X. Corrosion behavior of magnesium-graphene composites in sodium chloride solutions. J Magnesium Alloys 2017;5(3):271–6.
[177] Gusieva K, Davies C, Scully J, Birbilis N. Corrosion of magnesium alloys: the role of alloying. Int Mater Rev 2015;60(3):169–94.
[178] Fu W, Yang H, Li T, Sun J, Guo S, Fang D, Qin W, Ding X, Gao Y, Sun J. Enhancing corrosion resistance of ZK60 magnesium alloys via Ca microalloying: the impact of nanoscale precipitates. J Magnesium Alloys 2023;11(9):3214–30.
[179] Yin Z-Z, Qi W-C, Zeng R-C, Chen X-B, Gu C-D, Guan S-K, Zheng Y-F. Advances in coatings on biodegradable magnesium alloys. J Magnesium Alloys 2020;8(1): 42–65.
[180] Gray J, Luan B. Protective coatings on magnesium and its alloys—a critical review. J Alloys Compd 2002;336(1–2):88–113.
[181] Hu R-G, Zhang S, Bu J-F, Lin C-J, Song G-L. Recent progress in corrosion protection of magnesium alloys by organic coatings. Prog Org Coating 2012;73 (2–3):129–41.
[182] Ge M, Xie D, Yang Y, Liang H, Jiao C, Ye Y, Wu J, Yu H, Tian Z. Additive manufacturing a novel bioceramic bone scaffold with MgO/Ca3 (PO4) 2: microstructure, mechanical property and controllable degradation behavior. J Mater Res Technol 2023;27:2249–63.
[183] Liu J, Song D, Zhang L, Yang X, Zhu X, Sun W, Chen F. Microstructure and compressive properties of solution heat-treated magnesium-Mg2Si in-situ composite foams after complex modification. J Mater Res Technol 2021;15: 3673–82.
[184] Qu H, Rao D, Cui J, Gupta N, Wang H, Chen Y, Li A, Pan L. Mg-matrix syntactic foam filled with alumina hollow spheres coated by MgO synthesized with solution coating-sintering. J Mater Res Technol 2023;24:2357–71.
[185] Bhosale D, Georgy K, Mukherjee M, Kumar GV. Production, stability and properties of ultrafine MgAl2O4 (spinel) particles stabilized Mg–3Ca alloy foams. J Mater Res Technol 2024;28:4012–24.
[186] Ahmadi M, Tabary SB, Rahmatabadi D, Ebrahimi M, Abrinia K, Hashemi R. Review of selective laser melting of magnesium alloys: advantages, microstructure and mechanical characterizations, defects, challenges, and applications. J Mater Res Technol 2022;19:1537–62.
[187] Chen C, Li S, Ling C, Yang Y, Gao C, Li Y, Xiao X, Zhou W, Shuai C. Laser printed amorphous magnesium alloy: microstructure, mechanical properties and degradation behavior. J Mater Res Technol 2023;27:6961–73.
[188] Li Y, Zhang A, Li C, Xie H, Jiang B, Dong Z, Jin P, Pan F. Recent advances of high strength Mg-RE alloys: alloy development, forming and application. J Mater Res Technol 2023. In Press.
[189] Mehdizade M, Eivani AR, Asgari H, Naghshin Y, Jafarian HR. Assessment of microstructure, biocompatibility and in-vitro biodegradation of a biomedical Mg-Hydroxyapatite composite for bone tissue engineering. J Mater Res Technol 2023; 27:852–75.
[190] Gao Y, Ying L, Fan Z, Wei Y. The failure behavior of syntactic foams as buoyancy materials for deepsea applications. Eur J Mech Solid 2024 Feb 5:105256.
[191] Abazari S, Shamsipur A, Bakhsheshi-Rad HR, Ismail AF, Sharif S, et al. Carbon nanotubes (CNTs)-Reinforced magnesium-based matrix composites: a comprehensive review. Materials 2020;13:4421.
[192] Liu J, Sun W, Zheng Z, Xiao X, Che C, Cheng L, Zhu X, Liu X. Enhancing compressive properties and sound absorption characteristic of open-cell Mg foams through plasma electrolytic oxidation treatment. J Mater Res Technol 2023;25: 1263–72.

Jarosław Drelich is a professor of materials science at Michigan Technological University (Houghton, Michigan). He also holds an adjunct professorship in the department of Chemical and Materials Engineering at the University of Alberta (Alberta, Canada). He is known primarily for his contributions to the field of wetting phenomena, which include the effect of drop/bubble size on apparent contact angle on a rough surface, in addition to fundamental work on structured hydrophilic/hydrophobic alternating surfaces. Drelich has authored more than 130 scientific papers and 8 patents. He has an h-index of 67 and according to Google Scholar, his articles have been cited over 15538 times. Drelich is a member of the External Advisory Board for the Journal of Adhesion Science and Technology and founding editor-in-chief of the journal Surface Innovations.

Hamid Reza Bakhsheshi-Rad earned his Ph.D. in materials engineering from Universiti Teknologi Malaysia (UTM) in 2013. He is an associate professor in the Department of Materials Engineering at Najafabad Branch, Islamic Azad University, Iran. He has an h-index of 51 and according to Google Scholar, his articles have been cited over 7761 times. His research interests include new biodegradable magnesium, zinc, and their alloys, additive manufacturing and scaffolds for biomedical applications, surface modification, and nanocomposites.